AUTOPHAGY
2024, VOL. 20, NO. 1, 94–113
https://doi.org/10.1080/15548627.2023.2249750

RESEARCH PAPER

Disrupted endoplasmic reticulum-mediated autophagosomal biogenesis in a *Drosophila* model of C9-ALS-FTD

Hyun Sung [a,b] and Thomas E. Lloyd [a,b]

[a]Department of Neurology, School of Medicine, Johns Hopkins University, Baltimore, MD, USA; [b]The Solomon H. Snyder Department of Neuroscience, School of Medicine, Johns Hopkins University, Baltimore, MD, USA

ABSTRACT

Macroautophagy/autophagy is a major pathway for the clearance of protein aggregates and damaged organelles, and multiple intracellular organelles participate in the process of autophagy, from autophagosome formation to maturation and degradation. Dysregulation of the autophagy pathway has been implicated in the pathogenesis of neurodegenerative diseases including amyotrophic lateral sclerosis (ALS) and frontotemporal dementia (FTD), however the mechanisms underlying autophagy impairment in these diseases are incompletely understood. Since the expansion of GGGGCC (G_4C_2) repeats in the first intron of the *C9orf72* gene is the most common inherited cause of both ALS and FTD (C9-ALS-FTD), we investigated autophagosome dynamics in *Drosophila* motor neurons expressing 30 G_4C_2 repeats (30 R). *In vivo* imaging demonstrates that expression of expanded G_4C_2 repeats markedly impairs biogenesis of autophagosomes at synaptic termini, whereas trafficking and maturation of axonal autophagosomes are unaffected. Motor neurons expressing 30 R display marked disruption in endoplasmic reticulum (ER) structure and dynamics in the soma, axons, and synapses. Disruption of ER morphology with mutations in Rtnl1 (Reticulon-like 1) or atl (atlastin) also impairs autophagosome formation in motor neurons, suggesting that ER integrity is critical for autophagosome formation. Furthermore, live imaging demonstrates that autophagosomes are generated from dynamic ER tubules at synaptic boutons, and this process fails to occur in a C9-ALS-FTD model. Together, these findings suggest that dynamic ER tubules are required for formation of autophagosomes at the neuromuscular junction, and that this process is disrupted by expanded G_4C_2 repeats that cause ALS-FTD.

Abbreviations: 3R: UAS construct expressing 3 G_4C_2 repeats (used as control); 3WJ: three-way junction; 12R: UAS construct expressing leader sequence and 12 G_4C_2 repeats; 30R: UAS construct expressing 30 G_4C_2 repeats; 36R: UAS construct expressing 36 G_4C_2 repeats; 44R: UAS construct expressing leader sequence and 44 G_4C_2 repeats; ALS: amyotrophic lateral sclerosis; Atg: autophagy related; atl: atlastin; C9-ALS-FTD: ALS or FTD caused by hexanuleotide repeat expansion in *C9orf72*; ER: endoplasmic reticulum; FTD: frontotemporal dementia; HRE: GGGGCC hexanucleotide repeat expansion; HSP: hereditary spastic paraplegia; Lamp1: lysosomal associated membrane protein 1; MT: microtubule; NMJ: neuromuscular junction; Rab: Ras-associated binding GTPase; RAN: repeat associated non-AUG (RAN) translation; RO-36: UAS construct expression "RNA-only" version of 36 G_4C_2 repeats in which stop codons in all six reading frames are inserted.; Rtnl1: Reticulon-like 1; SN: segmental nerve; TFEB/Mitf: transcription factor EB/microphthalmia associated transcription factor (*Drosophila* ortholog of TFEB); TrpA1: transient receptor potential cation channel A1; VAPB: VAMP associated protein B and C; VNC: ventral nerve cord (spinal cord in *Drosophila* larvae)

ARTICLE HISTORY
Received 10 April 2023
Revised 8 August 2023
Accepted 11 August 2023

KEYWORDS
Autophagy; axonal transport; C9-ALS-FTD; Drosophila; endoplasmic reticulum (ER) dynamics; motor neuron

Introduction

In neurons, efficient clearance of aggregated proteins and dysfunctional organelles is essential to meet cellular extremes in metabolism and longevity, particularly motor neurons which have long, large diameter axons. For this reason, neurons are highly dependent on macroautophagy (hereafter referred to as autophagy) to maintain protein and organelle homeostasis [1–4], and thus, defective autophagy has been heavily implicated in the pathogenesis of neurodegenerative diseases [5–8]. Due to their polarized morphology and compartmentalized cellular functions, neurons are critically reliant on robust spatiotemporal regulation of organelle dynamics in the autophagy pathway [9–11]. The soma is thought to be the primary site of major degradative pathways and is enriched in acidified lysosomes [12–15], whereas presynaptic terminals, responsible for signal transmission, are the primary site of autophagy initiation and autophagosome formation [9,16–18]. The precise spatial and temporal regulation of the autophagy pathway during retrograde axonal transport, from autophagosomal biogenesis to autolysosomal maturation and degradation [16,17,19,20], are likely to be especially critical in neurons with extremely long axons, such as human motor axons that may be up to a meter in length.

CONTACT Hyun Sung hsung9@jhmi.edu Department of Neurology and Neuroscience, School of Medicine, Johns Hopkins University, 855 N. Wolfe St., Rangos 294, Baltimore, MD 21205, USA; Thomas E. Lloyd tlloyd4@jhmi.edu Department of Neurology and Neuroscience, School of Medicine, Johns Hopkins University, 855 N. Wolfe St., Rangos 290, Baltimore MD 21205, USA

This article has been corrected with minor changes. These changes do not impact the academic content of the article.
Supplemental data for this article can be accessed online at https://doi.org/10.1080/15548627.2023.2249750

Although autophagy has been widely investigated as a cellular catabolic process that can be triggered by starvation in non-neuronal cells [21–23], biogenesis of neuronal autophagosomes is thought to occur primarily in a constitutive manner at the distal neurite [10,16]. The main source of autophagic membranes at the presynaptic terminal remains unclear, and many distinct membrane compartments, including synaptic vesicles, mitochondria, plasma membranes, and the endoplasmic reticulum (ER) [24–26], have been suggested to contribute to phagophore generation. Unlike other intracellular organelles, ER forms a continuous structure throughout the neuron [27], and thus the ER has been suggested to spatially regulate autophagy [9,28]. Due to its physical continuity with dynamic ER tubule growth, retraction and rearrangement, axonal ER is a potential platform for the coordination of multiple steps in autophagosomal processes, from autophagosome formation [9,29–31] to transport [32–34] and maturation [32,35]. In neurons, the underlying mechanisms of how ER structure and dynamics impact the autophagy pathway remain unclear. Because mutations in genes encoding ER membrane proteins cause neurodegenerative diseases affecting motor neurons including hereditary spastic paraplegias (HSPs) [36–38] and amyotrophic lateral sclerosis (ALS) [39,40], altered ER function may contribute to the pathogenesis of neurodegenerative diseases.

ALS is a neurodegenerative disease characterized by the degeneration of upper and lower motor neurons leading to muscle weakness and atrophy [41–43], and it shares a range of genetic, cellular and pathologic features with frontotemporal dementia (FTD) [44–46]. Like many neurodegenerative disorders, key pathological hallmarks of ALS and FTD include the presence of cytoplasmic protein inclusions, suggesting disrupted neuronal proteostasis in affected neurons [47–50]. Although the majority of ALS and FTD cases are sporadic, a GGGGCC (G_4C_2) hexanucleotide repeat expansion (HRE) in *C9orf72* is the most common inherited cause of ALS and FTD (C9-ALS-FTD) [51,52]. Haploinsufficiency of *C9orf72* may contribute to C9-ALS-FTD pathogenesis [51,53]; however, the preponderance of evidence indicates that disease results from gain-of-function toxicity from expression of the G_4C_2 repeat containing RNA molecules [54–56] and/or repeat-associated non-AUG (RAN) mediated translation of dipeptide repeat (DPR) proteins [57–59]. We previously demonstrated that expanded G_4C_2 repeats inhibit nucleocytoplasmic transport [60], and impaired nuclear localization of the transcription factor TFEB/Mitf causes impaired autolysosomal function [61]. As enhancing autophagic clearance and ER homeostasis recovery are promising therapeutic targets in ALS [62,63], an understanding of whether and how impaired autophagy is related to ER defects in C9-ALS-FTD model needs to be explored.

In this study of autophagy in *Drosophila* models of C9-ALS-FTD, we investigate an *in vivo* link between ER dynamics and autophagosomal biogenesis and test how G_4C_2 repeats alter autophagy in motor neurons. Expression of the G_4C_2 HRE in motor neurons leads to a specific reduction in autophagosomal number and a severe impairment in ER structure and dynamics. Despite this impairment in autophagosome biogenesis, autophagosome maturation and retrograde autophagosome axonal transport occur normally. Similarly, disruption of ER integrity by expressing mutations in reticulon or atlastin impairs autophagosome formation. Importantly, we find that autophagosomal biogenesis at presynaptic terminals is spatiotemporally associated with dynamic ER tubules, and our *in vivo* data suggest that defective ER dynamics in C9-ALS-FTD models impairs autophagosome formation. Taken together, our findings suggest that an impairment in ER dynamics leads to a disruption of autophagy initiation in C9-ALS-FTD and emphasize an important role for the ER in autophagy regulation at synapses.

Results

Expanded G_4C_2 repeat expression inhibits axonal autophagosomal flux without impairing retrograde transport

We previously demonstrated that expression of an expanded G_4C_2 repeat disrupts nucleocytoplasmic transport [60], leading to cytoplasmic mislocalization of the transcription factor TFEB/Mitf [61]. Since defects in axonal transport and autophagy are implicated in the pathogenesis of neurodegenerative diseases [64–66], we hypothesized that altered axonal transport of autophagosomes might underlie neuronal vulnerability in C9-ALS-FTD. Axonal autophagosomes were visualized in motor neurons of the intact *Drosophila* larval nervous system by expressing mCherry-Atg8a under control of *VGlut-GAL4*, and their traffic was monitored *in vivo* [11]. Consistent with our previous observation of a reduced number of autophagic vesicles in motor neuron cell bodies [61], there is a pronounced loss of autophagosomes in axons of motor neurons expressing 30 G_4C_2 repeats (30 R) (Figure 1A,B; Movie S1,S2). To confirm that the reduction in axonal autophagosome density observed with 30 R expression is caused by expression of G_4C_2 repeats, we also examined axonal autophagosome density in motor axons expressing 3 R, 36 R, or an "RNA-only" version of 36 R (RO-36) in which RAN translation is inhibited by the introduction of stop codons [67]. There was a significant reduction of autophagosomal density in axons expressing 36 R compared to those expressing either 3 R or RO-36 (Fig. S1A,B), demonstrating that uninterrupted, expanded repeats are required for autophagosome inhibition. Thus, expression of a pathologic G_4C_2 repeat expansion reduces autophagosomal density in *Drosophila* motor axons.

Next, we assessed axonal autophagosome motility to determine whether the reduction in autophagosome density in 30 R-expressing axons is accompanied by alterations in transport. Consistent with our prior observation [11], the majority of neuronal autophagosomes travel retrogradely in control motor axons (Figure 1C). However, retrograde autophagosomal flux was severely reduced in 30 R-expressing axons (Figure 1D). Next, we quantified additional parameters of autophagosomal movement in axons including velocity, run length, and duty cycle, and found that none of these parameters were affected in 30 R-expressing neurons (Figure 1E-H). Indeed, autophagosomal motility dynamics and the percentage of motile autophagosomes in axons were unchanged by 30 R expression. These data indicate that the reduced autophagosomal flux seen in 30 R-expressing fly motor axons results from

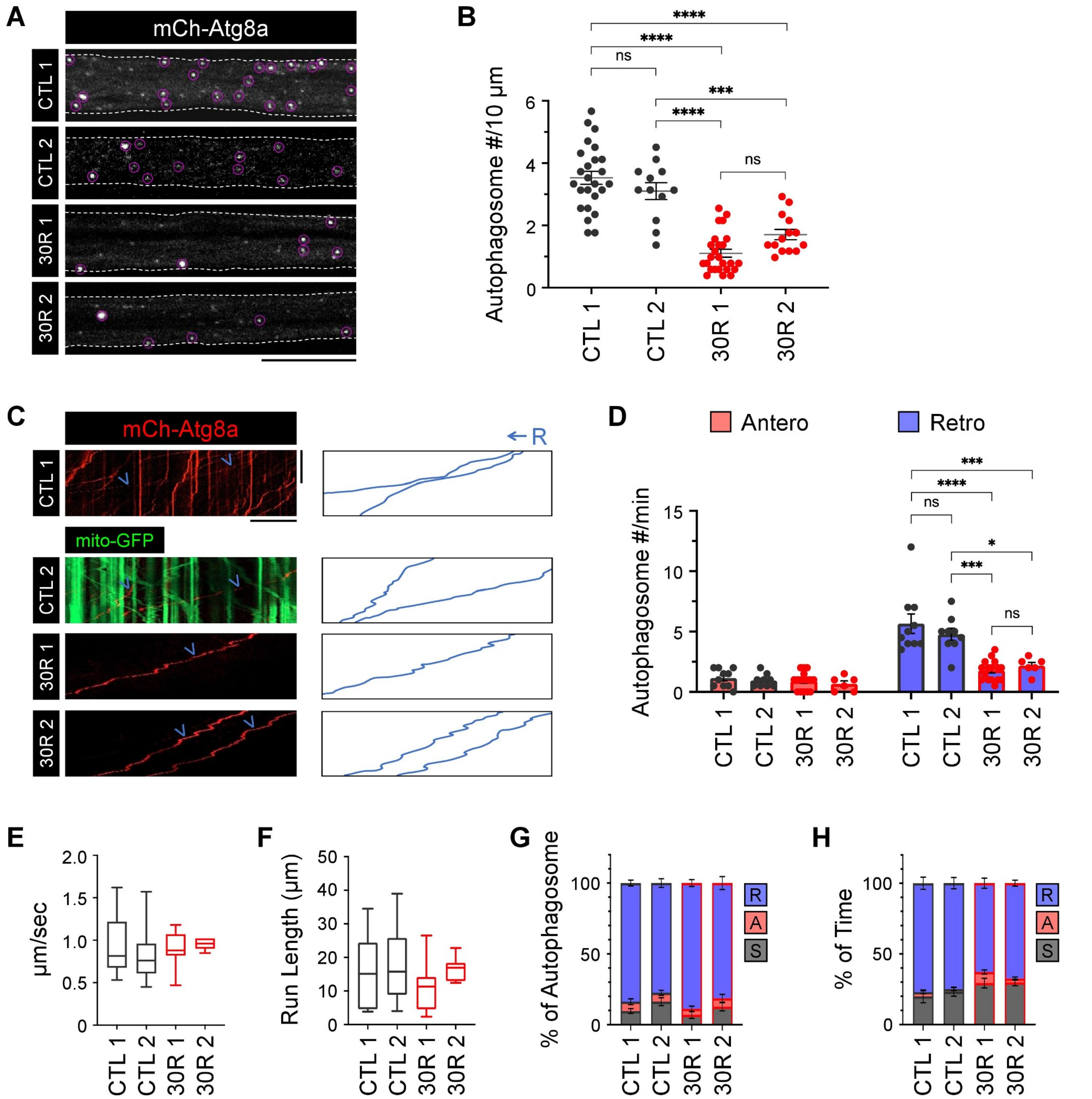

Figure 1. Expression of 30 G_4C_2 repeats (30 R) reduces motor axon autophagosomes without altering motility. (A) autophagosomes, labeled with mCherry (mCh)-tagged Atg8a, are imaged within motor axons of the third-instar larval segmental nerve. In control 1 (CTL 1), UAS-mCh-Atg8a is driven by *VGlut-GAL4*. In control 2 (CTL 2), mCherry-Atg8a is co-expressed with mito-GFP to control for GAL4/UAS dilution. Two independent UAS-$(G_4C_2)_{30}$ transgenic lines are used (30 R 1 on chromosome 3 and 30 R 2 on chromosome 2). White dashed lines denote boundaries of segmental nerves. Scale bar: 10 μm. (B) quantification of autophagosomal density in motor axon. Number of animals in total; $n = 25$ (CTL 1), $n = 12$ (CTL 2), $n = 25$ (30 R 1) and $n = 14$ (30 R 2). (C) representative kymographs of autophagosome axonal transport in motor axons from the indicated genotypes. Blue angle brackets indicate retrograde transport of autophagosomes. Scale bars: 1 min (vertical) and 10 μm (horizontal). Axonal transport of autophagosomes is analyzed by measuring: flux (D), the number of autophagosomes moving through axon cross-section per minute, velocity (E), run length (F), and percentage of autophagosomes that are moving (G) in the retrograde direction (R), anterograde direction (A), or stationary (S). (H) retrograde moving autophagosomes are individually analyzed by measuring duty cycle, the percentage of time spent moving in retrograde direction (R), anterograde direction (A), or stationary (S). Number of animals in total; $n = 10$ (CTL 1), $n = 9$ (CTL 2), $n = 16$ (30 R 1) and $n = 6$ (30 R 2). Error bars indicate mean ± SEM. Significance is determined by one-way ANOVA with Bonferroni's multiple comparisons test (B, D, E and F), and by Chi-Square test with a *post-hoc* analysis (G and H), respectively. *$p < 0.05$, ***$p < 0.001$, ****$p < 0.0001$, and ns = not significant.

a reduction in organelle density rather than changes in motility. An impairment in autophagosome number in axons could be due to a decrease in formation at distal axon termini, an increase in degradation or maturation of autophagosomes, or both.

Autophagosomal biogenesis is inhibited in motor synaptic terminals by expression of expanded G_4C_2 repeats

Though the mechanisms of autophagosome biogenesis in axons remains unclear, autophagosomes have been shown to

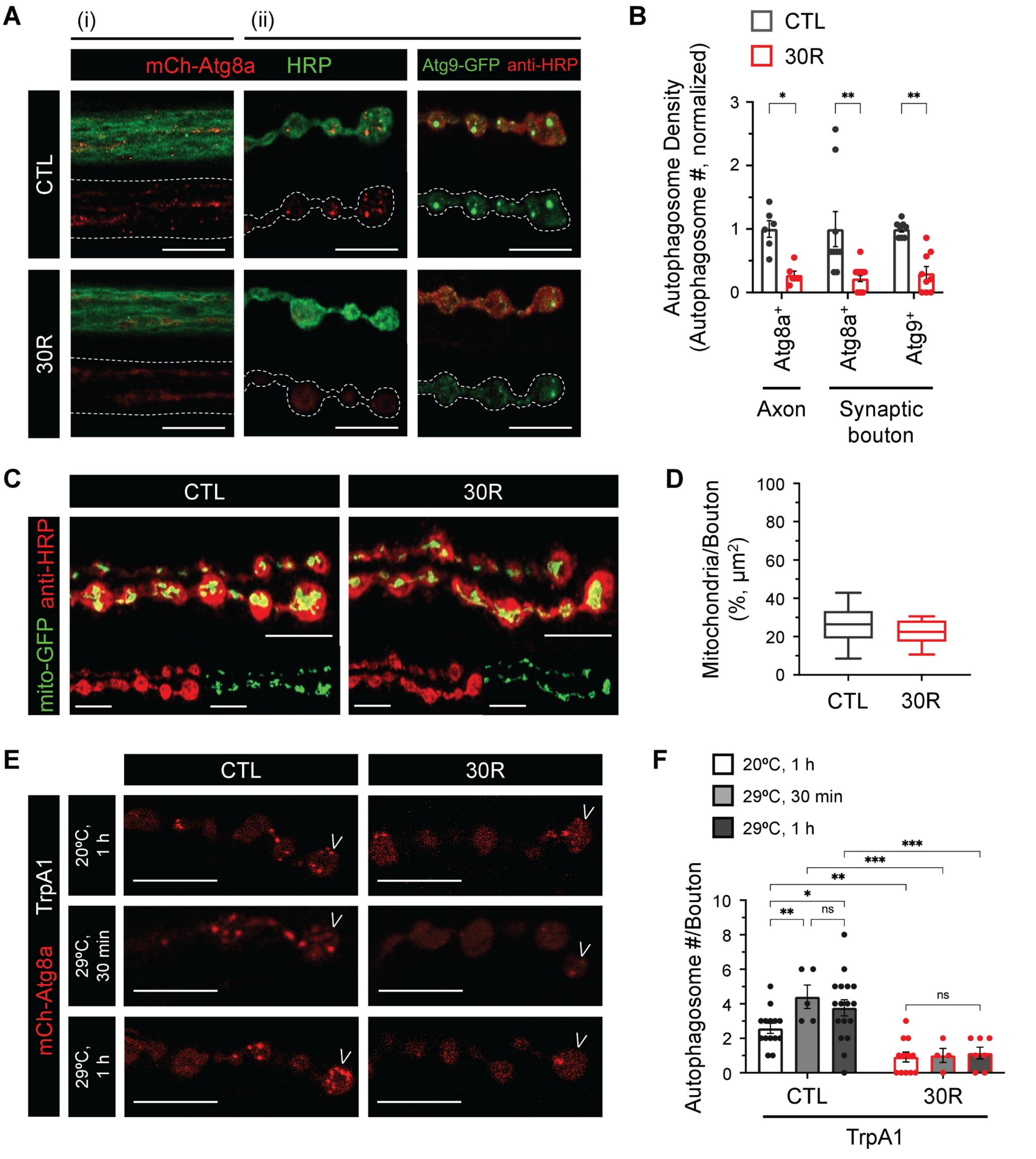

Figure 2. Autophagosome formation is inhibited in synaptic boutons in *Drosophila* models of C9-ALS-FTD. (A) representative images of autophagosomes in motor axons (i) and synaptic boutons (ii) from the indicated genotypes. Autophagic vesicles and preautophagosomal structures are visualized by Atg8a^{+} and Atg9^{+} signals respectively. anti-DsRed antibody immunostaining is used to amplify mCherry-Atg8a and anti-GFP is used to amplify Atg9-GFP. White dashed lines denote (i) motor axons and (ii) motor synaptic terminal boutons. Scale bars: 10 µm. (B) density of autophagosomes is quantified from motor axons and synaptic boutons. Number of animals in total; $n = 15$ (CTL) and $n = 22$ (30 R) for autophagic vesicle (Atg8a^{+}) analysis, and $n = 8$ (CTL) and $n = 9$ (30 R) for preautophagosomal structure (Atg9^{+}) analysis. (C) representative images of mitochondria in synaptic boutons from the indicated genotypes. Scale bars: 10 µm. (D) density of mitochondria is quantified by measuring mitochondrial area from motor synaptic boutons. Number of animals in total; $n = 32$ (CTL) and $n = 27$ (30 R). (E) representative synaptic boutons of the indicated genotypes without (20°C) or with (29°C) TrpA1 activation. Laval motor neurons are excited through activation of calcium permeable ion channel, TrpA1, by incubation at 29°C for either 30 min or 1 h. Synaptic terminal bouton is indicated by white angle bracket. Scale bars: 10 µm. (F) number of autophagosomes is quantified for autophagosomal density in a single terminal bouton. Number of animals in total; $n = 14$ (CTL in 20°C, 1 h), $n = 5$ (CTL in 29°C, 30 min), $n = 17$ (CTL in 29°C, 1 h), $n = 12$ (30 R in 20°C, 1 h), $n = 4$ (CTL in 29°C, 30 min) and $n = 7$ (30 R in 29°C, 1 h). Error bars indicate mean ± SEM. Significance is determined by unpaired two-tailed *t*-test (B and D), and by one-way ANOVA with Bonferroni's multiple comparisons test (F). $^{*}p < 0.05$, $^{**}p < 0.01$, $^{***}p < 0.001$, and ns = not significant.

be formed constitutively in the distal axon terminal [9,16,19,68]. Since autophagosomes in *Drosophila* motor neurons primarily form at synaptic boutons of the neuromuscular junction (NMJ), we investigated the localization of vesicles positive for Atg8a and Atg9, the only known integral membrane protein present on preautophagosomal structures [18,69,70]. We found that 30 R expression caused a severe reduction in the number of Atg8a$^+$ autophagosomes in both axons and synaptic boutons and also led to a reduction in Atg9-GFP-positive punctae at synaptic boutons (Figure 2A,B). Importantly, there was not a generalized reduction of organelles at the NMJ, as 30 R expression did not reduce mitochondrial density at synaptic boutons (Figure 2C,D), consistent with our previous finding that mitochondrial trafficking in motor axons occurs normally [71]. Together with our prior analyses of the motor neuron soma [61], these data indicate that 30 R expression leads to a severe impairment in autophagosome formation throughout motor neurons.

Previous studies in fly motor neurons have shown that neuronal stimulation increases autophagosome biogenesis in presynaptic terminals [18]. Thus, we reasoned that if 30 R expression down-regulates autophagosomal biogenesis, then it may also block autophagosome formation induced by neuronal activation in synaptic boutons. To test this hypothesis, we overexpressed the temperature-sensitive TrpA1 (Transient receptor potential cation channel A1) in motor neurons, and shifted the animals to 29°C for either 30 min or 1 h to stimulate neuronal activity [18,72]. Without TrpA1 expression, incubating control animals at 29°C for 30 min did not affect neuronal autophagy, though 1-h incubation slightly increased presynaptic autophagosome number (Fig. S2A,B). As previously described, however, induction of action potentials via TrpA1 activation increased the formation of Atg8a$^+$ autophagic vesicles in synaptic boutons of control animals (Figure 2E,F). In contrast, TrpA1 activation failed to increase autophagosome formation in animals expressing 30 R. Therefore, our results indicate that 30 R expression prevents neuronal activity-mediated autophagosome formation at the synapse, which consequently reduces the number of retrogradely-moving autophagosomes in motor axons.

Autophagosome maturation is unaffected by expanded G_4C_2 repeat expression

Studies from non-neuronal cells have shown that autophagosomes strongly colocalize with late endosomes and/or lysosomes, ultimately maturing into amphisomes and/or autolysosomes [73]. In addition, studies in embryonic neurons *in vitro* [16] as well as in fly neurons *in vivo* [17] have shown that retrograde movement of autophagosomes is tightly coupled with organelle maturation. Thus, we asked whether autophagosomes mature properly as they move retrogradely along axons in 30 R-expressing motor neurons. To examine autophagosome maturation, we visualized axonal amphisomes and autolysosomes in fly motor neurons by co-expressing mCherry-Atg8a with Rab7-GFP and with GFP-Lamp1, respectively, under the control of *VGlut-GAL4* (Figure 3A; Movie S3-S6). Organelles double-positive for Atg8a and Rab7 (amphisomes) or for Atg8a and Lamp1 (autolysosomes) primarily moved retrogradely in fly motor axons, and 30 R expression did not affect their retrograde velocity (Figure 3B) or run length (Figure 3C). Interestingly, despite the reduced density of autophagosomes in 30 R-expressing axons compared to control axons, the proportion of motile autophagosomes that fuse successfully with late endosomes (38.46% vs 32.75%) or lysosomes (15.28% vs 8.40%) were not significantly different (Figure 3D). These findings are consistent with a model in which autophagosome fusion with late endosomes is required for robust retrograde motility [74]. Collectively, our results indicate that while autophagosome biogenesis is severely reduced in 30 R-expressing neurons, autophagosome fusion and maturation is preserved to enable retrograde transport of the remaining autophagosomes.

ER integrity is impaired in Drosophila motor neurons expressing expanded G_4C_2 repeats

Since the endoplasmic reticulum (ER) has been suggested to contribute to autophagosome generation [9,28], and mutations in genes regulating ER structure and dynamics are implicated in ALS pathogenesis [75,76], we hypothesized that impaired autophagosome biogenesis in C9-ALS-FTD could be caused by alterations in the ER network. Indeed, the ER is the source of the earliest distinguishable autophagic structures in mammalian and fly cells [29,30]. Therefore, we examined the ER network in motor neurons *in vivo* to test whether altered ER integrity might contribute to defective autophagosome biogenesis in neurons expressing expanded G_4C_2 repeats. To visualize ER architecture *in vivo*, we expressed an ER retention signal (HDEL) fused with a *Drosophila* Hsc70–3/BiP (Heat shock protein 70 cognate 3) and Superfolder GFP (sfGFP) in motor neurons (sfGFP-HDEL), as previously described [77]. ER from control animals formed a reticular structure with a network of tubules in motor neurons (Figure 4A; i-iii), whereas ER in animals expressing 30 R displayed disrupted morphology with ER knots (clustered ER network) in cell bodies and ER discontinuities in axons and neuromuscular junctions (Figure 4A; iv-vi). To define the alterations in ER structure, we quantified ER tubule three-way junction (3WJ) density in cell bodies and the number of ER tubule fragments at synapses [78]. This analysis showed a significant reduction of ER 3WJ density (Figure 4B, C) and a marked increase of ER fragment number (Figure 4D, E) in 30 R-expressing motor neurons. Similarly, these morphological ER defects were also observed using additional fluorescent ER markers including Lys-GFP-KDEL for ER lumen and tdTomato-Sec61β for ER membrane in 30 R-expressing neurons (Fig. S3A,B).

To determine whether the ER and autophagosome impairments persistent into adulthood, we also examined these organelles in adult fly motor neurons. In motor neurons of the adult ventral nerve cord (VNC), 30 R expression significantly altered the ER morphology and reduced the autophagosome density (Figure 5A-C), similar to what was observed in larval motor neurons. Since newly formed adults are paralyzed in 30 R animals, we are unable to determine if this

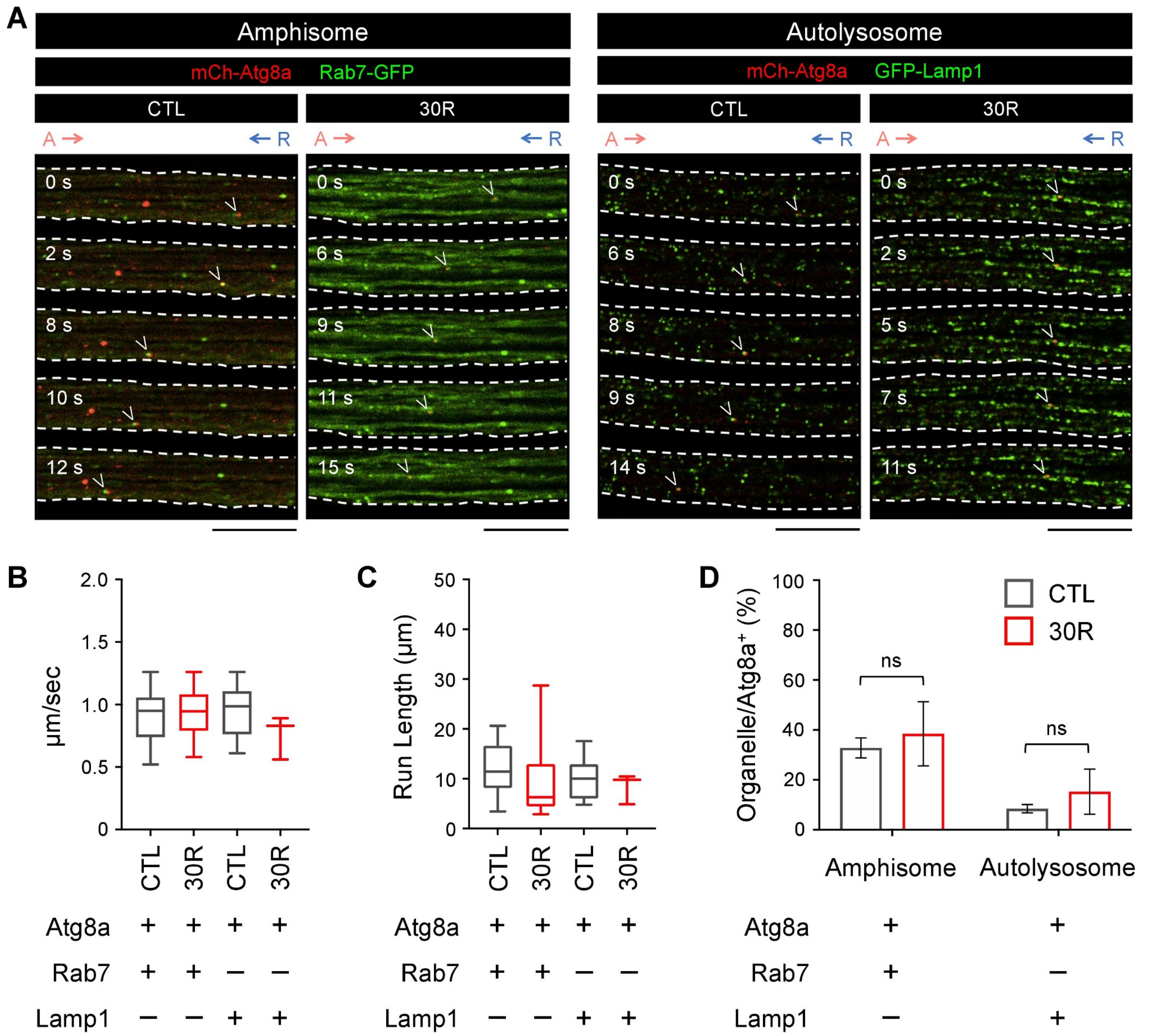

Figure 3. Autophagosomal maturation occurs normally in motor axons expressing 30 G_4C_2 repeats (30 R). (A) representative time-lapse images of axonal transport of amphisomes and autolysosomes in fly motor neurons. White angle brackets denote retrograde moving organelles that are visualized by co-expressing either mCherry-Atg8a with Rab7-GFP for amphisomes or mCherry-Atg8a with GFP-Lamp1 for autolysosomes. White dashed lines denote segmental nerves. Scale bars: 10 µm. Axonal transport of organelles is analyzed by measuring velocity (B) and run length (C). (D) quantitative ratio of organelle to autophagosome in motor axons. Number of animals in total; $n = 22$ (CTL for $Atg8^+$ and $Rab7^+$), $n = 13$ (CTL for $Atg8a^+$ and $Lamp1^+$), $n = 13$ (30 R for $Atg8a^+$ and $Rab7^+$) and $n = 12$ (30 R for $Atg8a^+$ and $Lamp1^+$). Error bars indicate mean ± SEM. Significance is determined by unpaired two-tailed *t*-test (B, C and D). ns = not significant.

phenotype becomes progressively worse with age. To determine if non-neuronal cells were affected, we analyzed the ER in the larval fat body and muscle cells and found that the ER in 30 R expressing non-neuronal cells was indistiguishable from controls (Figure 5D). Indeed, the periodic structure of the sarcoplasmic reticulum of 30 R-expressing larval muscles was unaffected (Figure 5E). Collectively, these data demonstrate that 30 R expression causes morphological disruption of the ER in *Drosophila* motor neurons.

Since live imaging demonstrates that the ER is remarkably dynamic [79–81], we next acquired time-lapse images of the ER to determine whether the morphological abnormalities are accompanied by alterations in ER motility. In 30 R-expressing motor neurons, disrupted ER dynamics was observed throughout the neuron, with severely impaired ER motility in cell bodies (Figure 6A and Fig. S4A,B; Movie S7, S8), axons (Figure 6B; Movie S9,S10) and synaptic termini (Figure 6C; Movie S11,S12). At NMJ synapses, where ER tubule growth and retraction was readily observed in control animals, there was a marked reduction of these dynamic events along with an increase in the number of static ER particles in 30 R-expressing animals (Figure 6D,E). Strikingly, though ER discontinuity was apparent and ER tubule growth and retraction events were rare, 30 R axons showed a preserved linear arrangement of axonal microtubules (MTs) (Fig. S3C), consistent with normal retrograde axonal transport of autophagosomes across ER discontinuities (Figure 6B; Movie S10). Thus, our results indicate that

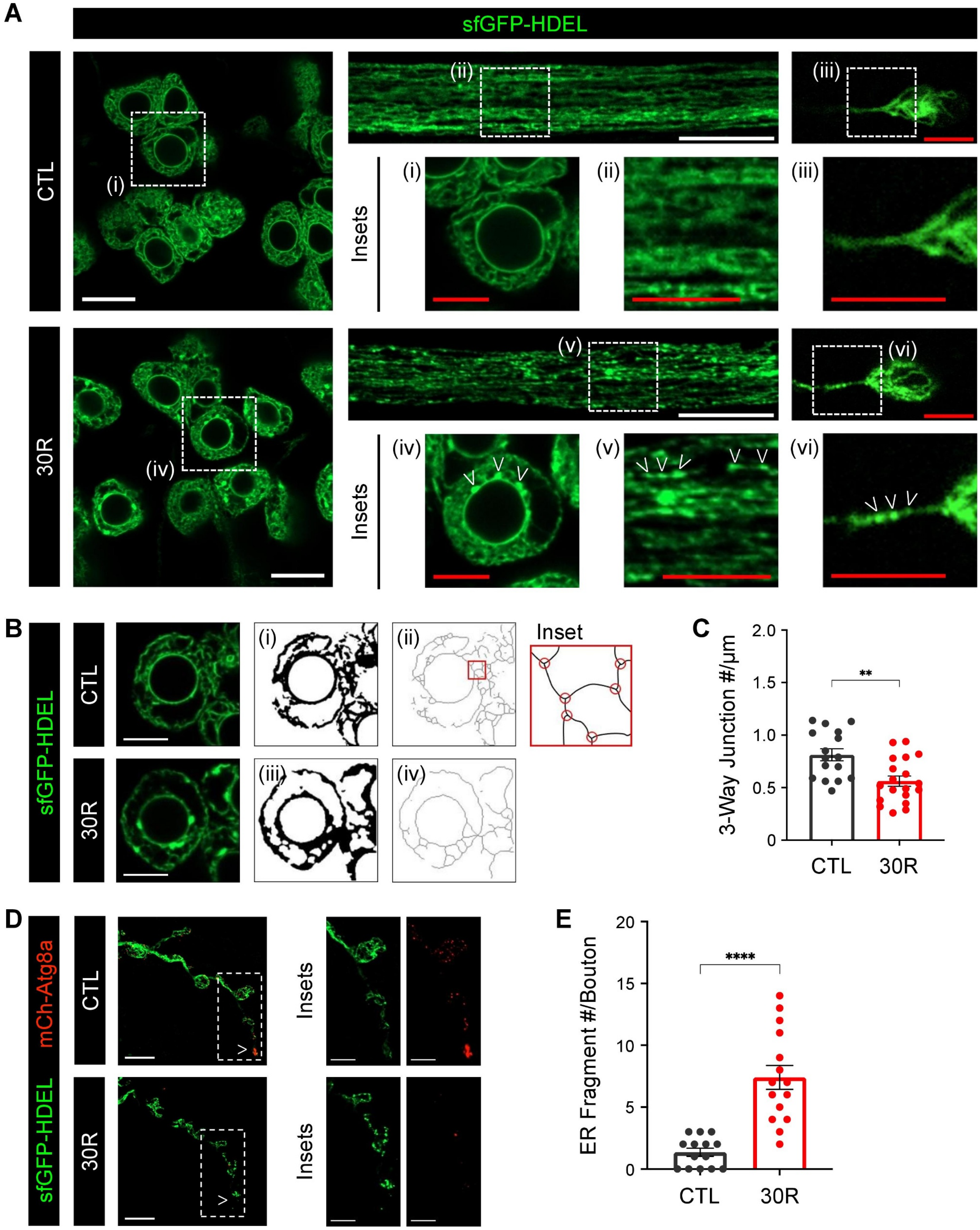

Figure 4. Expression of 30 G_4C_2 repeats (30 R) disrupts ER morphology throughout *Drosophila* larval motor neurons. (A) representative images of ER in motor neuronal soma (i and iv), axon (ii and v) and synaptic terminal (iii and vi) from the indicated genotypes. sfGFP-HDEL is used for imaging ER network. White angle brackets denote ER knots (iv), and ER discontinuity and fragmentation (v and vi). Scale bars: 10 μm (white) and 5 μm (red). (B) analysis of ER morphology and network in motor neuron cell bodies from the indicated genotypes. Images are binarized (i and iii) to acquire skeleton (ii and iv) of the ER network. Inset shows the skeleton of the ER network and three-way junctions (3WJs) between tubules (red circles). Scale bars: 5 μm. (C) in motor neuron cell bodies, ER network is quantified by measuring number of 3WJs per ER tubule length. Number of animals in total; $n = 16$ (CTL) and $n = 19$ (30 R). (D) representative images of ER and autophagosomes at the neuromuscular junction from indicated genotypes. White angle brackets denote terminal boutons. Scale bars: 10 μm and 5 μm (insets). (E) in motor synapses, ER structure is analyzed by measuring number of ER fragments per bouton. Number of animals in total; $n = 14$ (CTL) and $n = 15$ (30 R). Error bars indicate mean ± SEM. Significance is determined by unpaired two-tailed *t*-test (C and E). $^{**}p < 0.01$ and $^{****}p < 0.0001$.

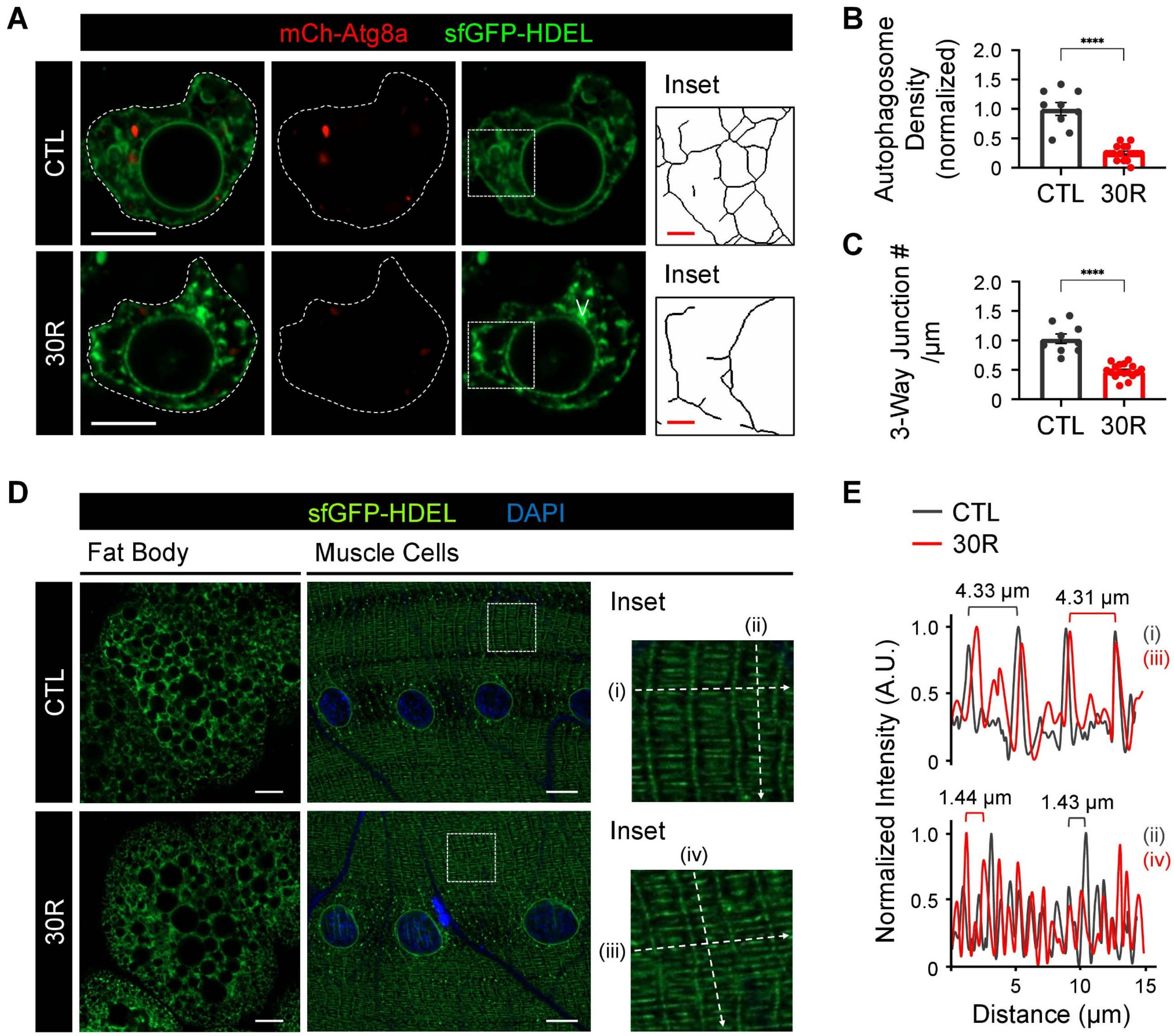

Figure 5. Expression of 30 G_4C_2 repeats (30 R) disrupts ER morphology specific to *Drosophila* motor neurons. (A) representative images of autophagosomes and ER in motor neuronal soma from the adult VNC. White angle bracket denotes ER knot and insets show the skeleton of the ER network from the indicated genotypes. Scale bars: 5 µm (white) and 1 µm (red). (B) density of autophagosomes is quantified from adult motor neuron cell bodies. Number of animals in total; $n = 8$ (CTL) and $n = 17$ (30 R). (C) in adult motor neuron cell bodies, ER network is quantified by measuring number of 3WJs per ER tubule length. Number of animals in total; $n = 8$ (CTL) and $n = 17$ (30 R). (D) representative images of ER in larval fat bodies and muscle cells from the indicated genotypes. Insets show the periodic structure of larval sarcoplasmic reticulum at horizontal (anteroposterior, i and iii) and vertical (lateral, ii and iv) axes. Scale bars: 10 µm. (E) signal intensity profiles of the sfGFP-HDEL are denoted from the dashed arrow lines in (D). The representative periodic distance of sarcoplasmic reticulum is indicated; 4.33 µm and 1.43 µm from control (i and ii) and 4.31 µm and 1.44 µm from 30 R (iii and iv) animals. Error bars indicate mean ± SEM. Significance is determined by unpaired two-tailed *t*-test (B and C). ****$p < 0.0001$.

30 R expression impairs ER structure and dynamics in motor neurons, without impeding MT-based organelle movements.

Autophagy is downregulated in Drosophila *larval motor neurons expressing disease-associated ER membrane proteins*

Given the inhibition of autophagosome biogenesis (Figure 2) and impaired ER integrity and dynamics (Figures 4, 5 and 6) in 30 R-expressing motor neurons, we further examined the relationship between these two processes using two additional fly models of C9-ALS-FTD, one expressing 36 R and the other expressing 44 R that also expresses GFP-tagged GR via RAN translation. In both the 36 R and 44 R models, we observed a similar alteration in the ER and reduction of autophagosomes as was observed in the 30 R model (Fig. S3D-F). In mouse hippocampal neurons, conditional knockout of the essential autophagy protein, Atg5, leads to accumulation of ER tubules in axons [82], suggesting a role for autophagy (reticulophagy) in limiting axonal ER. To test whether disruption of autophagy might directly impair ER dynamics in motor

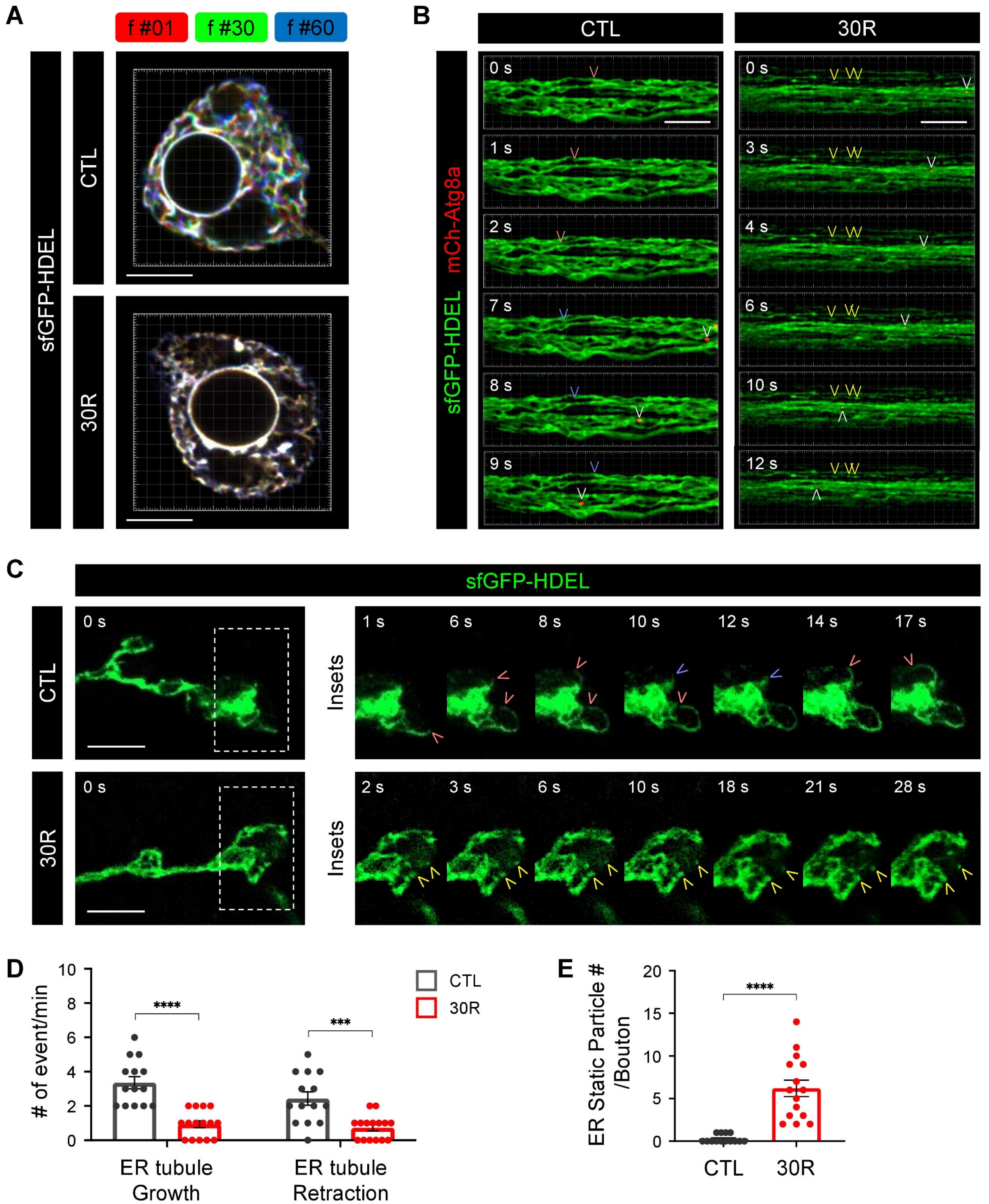

Figure 6. Expression of 30 G_4C_2 repeats (30 R) impairs ER dynamics in *Drosophila* motor neurons. (A) temporal color code of neuronal ER dynamics from the indicated genotypes. ER in motor neuronal soma was captured at 1 sec time intervals for 1 min. Single frames of pseudo-colored images were extracted from the time-lapse images for ER dynamics analysis; merged image of single ER network at indicated timepoint, $t = 1$ sec (red), $t = 30$ sec (green) and $t = 60$ sec (blue). With this representation, white ER tubules are static, whereas colored ER tubules are dynamic during the 1 min imaging. Reconstructed images are generated by Imaris 9.0.1 from the sections of 14.85 μm width (x) with 14.85 μm height (y). Scale bars: 5 μm. (B) axonal ER dynamic events from indicated genotypes. An example of ER tubule growth (red angle brackets), ER tubule retraction (blue angle brackets) and ER discontinuity (yellow angle brackets) are indicated. Axonal transport of autophagosomes (white angle brackets) is co-visualized with dynamic ER. Reconstructed images are generated by Imaris 9.0.1 from the sections of 25.27 μm width (x) with 9.95 μm height (y). Scale bars: 5 μm. (C) dynamics of neuronal ER in motor synaptic terminal from the indicated genotypes. An example of ER tubule growth (red angle brackets), ER tubule retraction (blue angle brackets) and ER fragmentation (yellow angle brackets) are indicated. Scale bars: 5 μm. Terminal ER dynamics is quantified by measuring number of events for ER tubule growth and retraction (D) and by measuring number of static ER particle per single bouton (E). Number of animals in total; $n = 14$ (CTL) and $n = 15$ (30 R). Error bars indicate mean ± SEM. Significance is determined by unpaired two-tailed *t*-test (D and E). ***$p < 0.001$ and ****$p < 0.0001$.

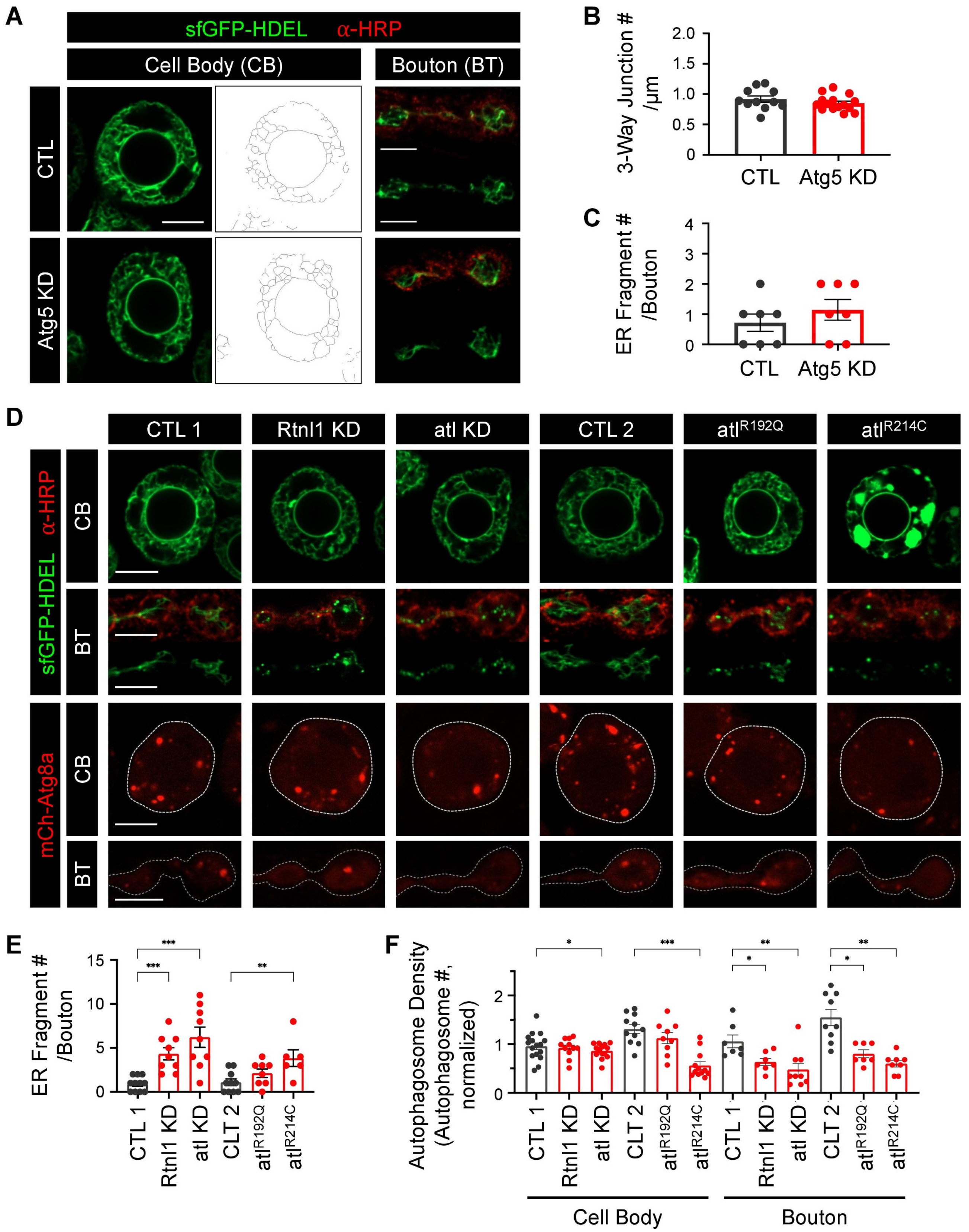

Figure 7. Expression of mutant ER membrane proteins inhibits autophagy in *Drosophila* motor neurons. (A) representative images of motor neuron ER in cell bodies (CB) and synaptic terminal boutons (BT) from the indicated genotypes. UAS-luciferase RNAi is used for control. Scale bars: 5 µm. ER morphology is analyzed by quantification of 3WJs in CB (B) and by quantification of ER fragments in BT (C). Number of animals in total; $n = 11$ (CTL) and $n = 15$ (Atg5 KD) for ER analysis in CB, and $n = 7$ (CTL) and $n = 7$ (Atg5 KD) for ER analysis in BT. (D) representative images of motor neuron ER and autophagosomes in cell bodies (CB) and synaptic terminal boutons (BT) from the indicated genotypes. UAS-luciferase RNAi is used for RNAi control (CTL 1), and UAS-lacZ is used for UAS overexpression control (CTL 2). White dashed lines denote motor neuron cell body and motor synaptic terminal. Scale bars: 5 µm. (E) in motor synapses, ER morphology is analyzed by quantifying the number of ER fragments in BT. Number of animals in total; $n = 11$ (CTL 1), $n = 9$ (Rtnl1 KD), $n = 9$ (atl KD), $n = 10$ (CTL 2), $n = 8$ (atl^{R192Q}), and $n = 6$ (atl^{R214C}). (F) density of autophagosomes is quantified from motor neuron CBs and BTs. Number of animals in total for CB/BT quantification; $n = 16/7$ (CTL 1), $n = 11/7$ (Rtnl1 KD), $n = 14/9$ (atl KD), $n = 11/9$ (CTL 2), $n = 9/7$ (atl^{R192Q}), and $n = 12/8$ (atl^{R214C}). Error bars indicate mean ± SEM. Significance is determined by unpaired two-tailed *t*-test (B and C), and by one-way ANOVA with Bonferroni's multiple comparisons test (E and F). $*p < 0.05$, $**p < 0.01$ and $***p < 0.001$.

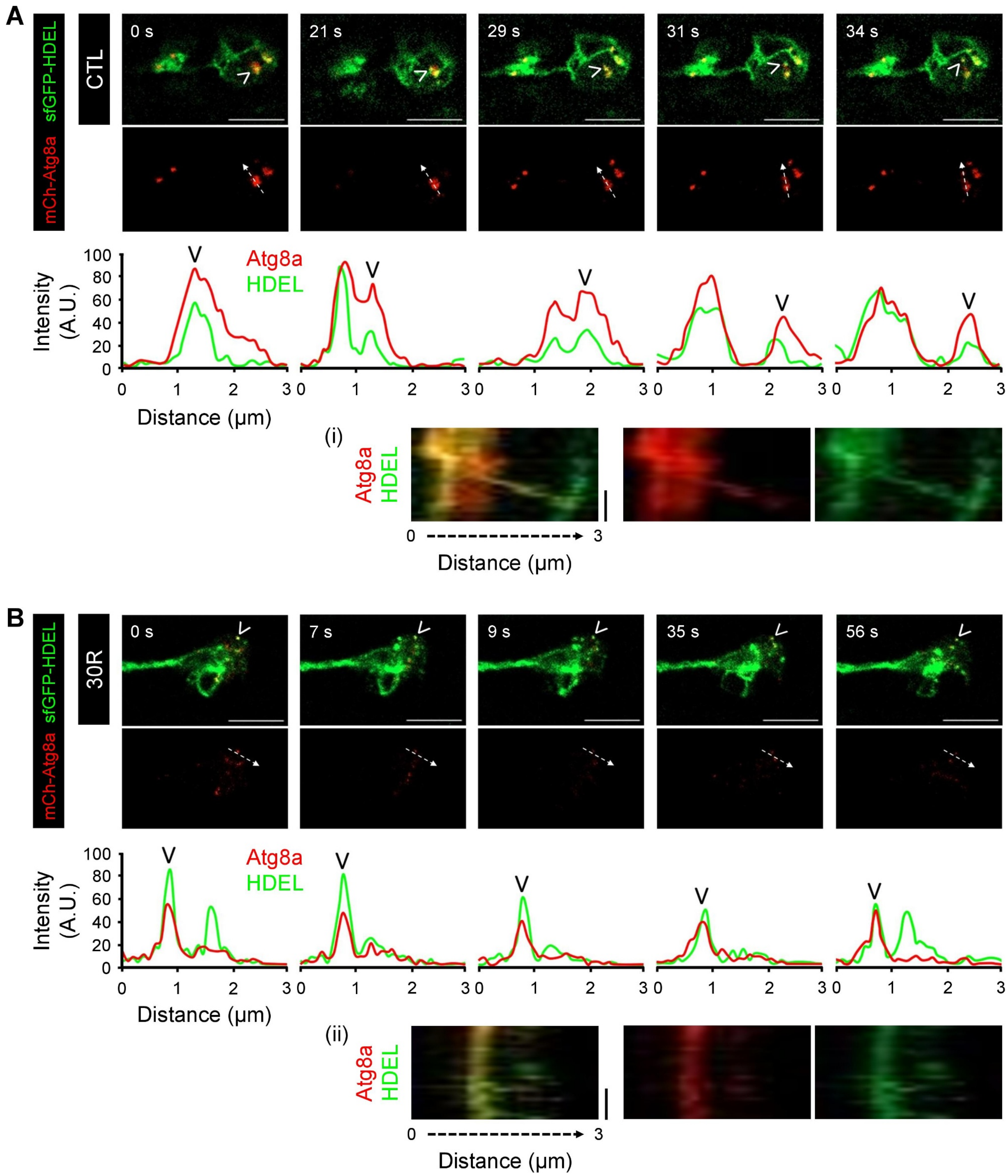

Figure 8. Developing autophagosomes co-migrate with ER at *Drosophila* terminal boutons. Time series of developing autophagomes with ER dynamics in terminal bouton of the distal motor axon. Two representative images are shown from the indicated genotypes, from control (A) and 30 R (B) animals. White angle brackets denote autophagosomal biogenesis events that co-localize and co-migrate with the ER tubule. Signal intensity profiles of line scans between mCherry-Atg8a and the sfGFP-HDEL are denoted from the dashed arrow lines, and black angle brackets denote the peak of Atg8a^{+} signals corresponding to white angle brackets on the images. Kymographs are generated from the corresponding dashed arrow lines on the images to display dynamics of ER and terminal autophagosomes *de novo*, from control (A, (i)) and 30 R (B, (ii)). Scale bars: 5 µm (horizontal) and 10 sec (vertical).

neurons, we analyzed ER morphology in cell bodies and synapses of flies coexpressing Atg5 RNAi. Quantitative RT-PCR confirmed a > 60% knockdown of *Atg5* gene expression in *Atg5* RNAi-expressing larvae (Fig. S5A), consistent with prior observations [83]. In fly motor neurons, Atg5 knockdown significantly reduced autophagosome number in both cell bodies and synaptic boutons (Fig. S5B,C). Despite this inhibition of autophagy, the morphology of

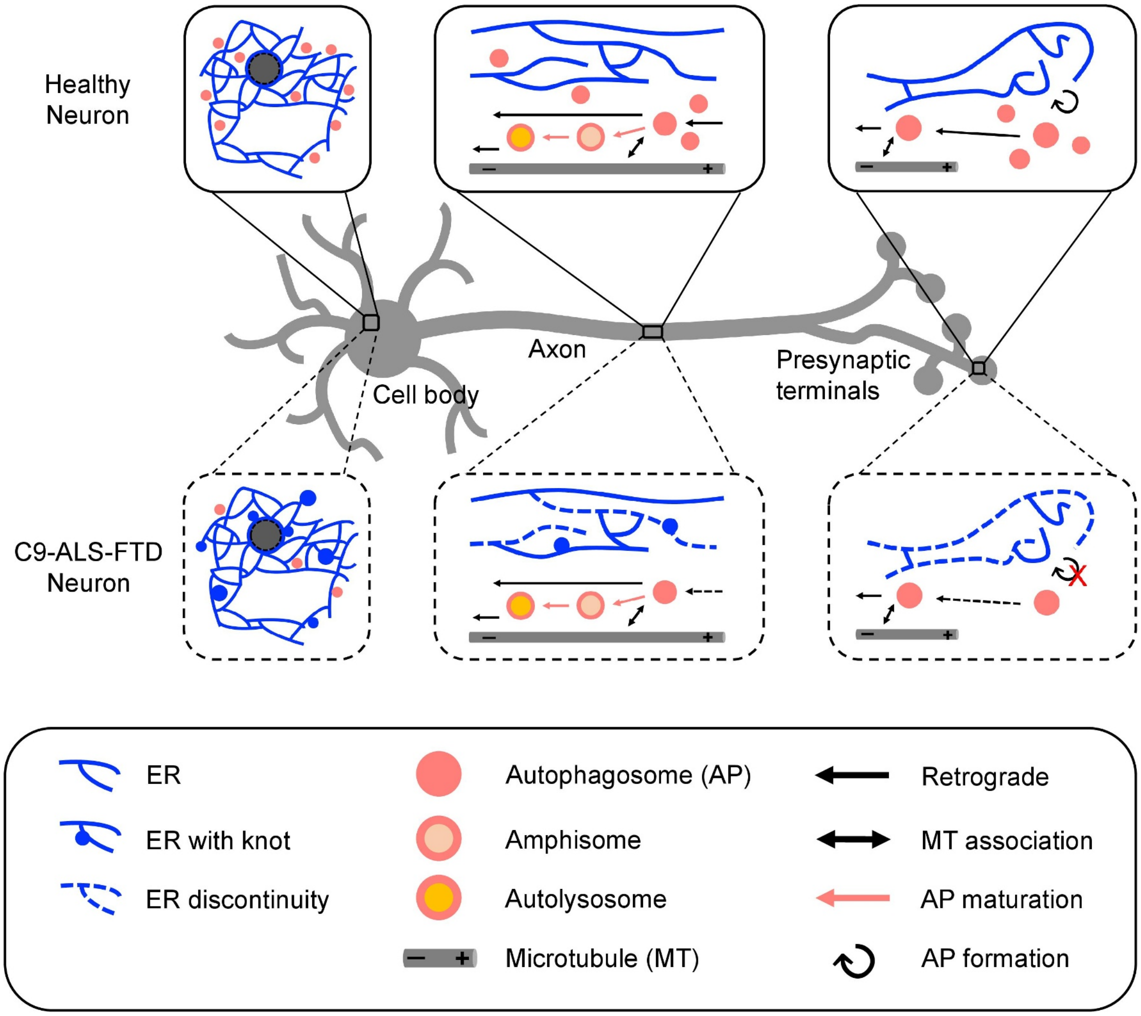

Figure 9. Schematic model for autophagosome biogenesis from dynamic ER tubules in healthy synapses and dysfunction in C9-ALS-FTD motor neurons. ER network is continuously distributed throughout the cytosol within motor neurons, including cell body, axon and presynaptic terminals. In healthy neurons, the ER is highly dynamic, with tubular extensions and retractions. Developing autophagosomes primarily form in distal axons from dynamic ER tubules in presynaptic terminals. In C9-ALS-FTD neurons, the ER is rigid, forming membrane "knots", tubule discontinuity, and fragmentation. This disrupted ER dynamics in C9-ALS-FTD neurons impairs formation of autophagosomes at synaptic boutons without impeding autophagosome maturation or retrograde transport. These defects in organelle dynamics eventually cause a reduction of autophagic vesicles in neuronal cell body (Cunningham KM et al., Elife 2020). ER; endoplasmic reticulum, AP; autophagosome, MT; microtubule.

the ER network and terminal ER tubule structure were not affected in motor neurons (Figure 7A-C). These results indicate that inhibition of autophagy is not sufficient to disrupt ER morphology in fly motor neurons, and suggest that impaired ER morphology is not caused by reduced autophagosome formation in 30 R-expressing animals.

An alternative hypothesis is that an impairment in autophagosome formation is caused by an impairment in ER tubule dynamics. Indeed, in cortical neurons from a mouse model of hereditary sensory and autonomous neuropathy, lack of axonal atlastin 3 (ATL3), an ER-network forming GTPase, resulted in fewer axonal autophagosomes, though it did not change axonal ER morphology [84]. In addition, it has been reported that depletion of ATL2 and ATL3 impairs the initial step of autophagosome formation [85]. Furthermore, recent data suggest that ER-derived vesicles, regulated by the endosomal sorting complex required for transport (ESCRT), facilitate the formation of autophagosomes in the *Drosophila* intestine [86]. To test whether alterations in ER morphology lead to an impairment in autophagosome formation in fly motor neurons, we performed multiple genetic manipulations known to disrupt the ER in flies, including knockdown of either Rtnl1, a *Drosophila* ortholog of RTN (reticulon), or ATL (atlastin) [78,79,87], and expression of HSP-associated atl mutations, atl^{R192Q} or atl^{R214C} [87]. In motor neuron cell bodies, while the ER network appeared slightly altered by Rtnl1 knockdown, there were no obvious changes with either atlastin knockdown or expression of atl^{R192Q} (Figure 7D and Fig. S5D,E). However, there was a severe disruption of the ER network structure in cell bodies expressing atl^{R214C}, as previously observed [87]. Next, we investigated the effects of these genetic manipulations on ER morphology in NMJ synaptic boutons. Interestingly, unlike motor neuron cell bodies, expression of Atl^{R214C} or knockdown of Rtnl1 or atl led to marked ER fragmentation at the presynaptic NMJ terminal (Figure 7D,E). These disruptions in ER morphology correlated with a reduction in autophagosome density (Fig. S5F), most notable at NMJ synaptic boutons (Figure 7D-F). In axons, defective ER structures were progressively apparent in distal axons, containing predominantly ER fragments with only sparse ER tubules (Fig. S5G). Collectively, our data indicate that ER integrity, especially distal axon ER tubule structure, is critical for autophagosome maintenance in fly motor neurons.

Expanded G_4C_2 repeat expression impedes ER-mediated autophagosome formation at the Drosophila *neuromuscular junction*

In primary neurons, autophagosome membranes are generated from ER at ZFYVE1/DFCP1 (zinc finger FYVE-type containing 1)-positive subdomains [9]. In *Drosophila* motor neurons expressing 30 R, we observed an inhibition of autophagosome biogenesis (Figure 2) as well as disrupted ER dynamics (Figure 6). We therefore hypothesized that the impairment in ER dynamics at synapses might directly impair autophagosome biogenesis. To determine whether neuronal autophagosomes form from dynamic ER tubules at synaptic boutons, we performed dual-color time-lapse confocal imaging of autophagosomes and the ER using mCherry-Atg8a and sfGFP-HDEL, respectively. Consistent with our previous observations, 30 R expression reduced the number of distal autophagosomes in NMJ synaptic boutons. In both 30 R and control animals, we noted that autophagosomes predominantly appeared on dynamic ER tubules as evidenced by $Atg8a^+$ signals coinciding with $HDEL^+$ signals (Figure 8A,B). Remarkably, at control terminal synaptic boutons, the emerging autophagosomes closely co-localized and co-migrated with ER (Figure 8A, (i); Movie S13), and migrating autophagosomes moved along with the tips of ER tubules (Fig. S6A; Movie S15). Though autophagosomes primarily colocalized with ER in 30 R-expressing animals, the autophagosomes in 30 R-expressing terminal boutons appear static, colocalizing with fragmented ER (Figure 8B, (ii) and Fig. S6B; Movie S14,S16). Together, these results provide *in vivo* evidence of a dynamic connection between distal autophagosomes and the ER, and suggest that developing autophagosomes form from dynamic ER tubules in *Drosophila* motor neuron synaptic boutons. These findings suggest that one mechanism whereby disease-associated G_4C_2 repeats impair neuronal autophagy is through disrupting ER dynamics and inhibiting autophagosome biogenesis (Figure 9).

Discussion

While autophagy has long been known to play an essential role in clearance of protein aggregates and prevention of neurodegeneration [5–8], much less is known about the spatiotemporal regulation of autophagy in neurons, particularly in axons and synapses [9–11]. Our previous study in fly models of C9-ALS-FTD, the most common genetic cause of these diseases, suggested that autophagy was disrupted in motor neuron cell bodies due to impaired nuclear import of the transcription factor TFEB/Mitf [61]. However, since neuronal autophagosomes primarily form at synapses, whether and how autophagy is disrupted in axons and synapses in C9-ALS-FTD has remained unclear. To better understand how autophagosomes form in synapses and are retrogradely trafficked along axons, we have performed live imaging in fly models of C9-ALS-FTD. We find that while autophagosomes fail to form normally at NMJ synapses, even with neuronal stimulation, they are able to mature and undergo retrograde axonal transport normally. Strikingly, our investigations of autophagosome biogenesis at synapses show that autophagosomes at the NMJ normally form at tips of dynamic ER tubules, and this process is severely disrupted in C9-ALS-FTD. Furthermore, ER integrity and dynamics are severely disrupted in our C9-ALS-FTD models, and mutations in reticulon and atlastin known to disrupt the ER also impair autophagosome formation. Together, these findings support a model (Figure 9) whereby dynamic ER tubules are required to form new autophagosomes at synapses prior to their retrograde axonal transport.

At the synapse, the precise mechanisms of how local machinery regulates biogenesis of autophagosomes remain unclear [88,89]. One key regulator of this process is Atg9, a transmembrane lipid scramblase present on Golgi-derived vesicles enriched at synaptic sites [18,19]. Atg9-containing vesicles undergo exo-endocytosis at synapses and enable the expansion of the isolation membrane critical for autophagosome formation [70]. In *Drosophila* NMJ synaptic boutons, we observe large $Atg9\text{-}GFP^+$ structures within synaptic boutons, and these vesicles are dramatically reduced with 30 R expression (Figure 2A,B). A recent study suggests a role for $Atg9^+$ vesicles in phase separation of RB1CC1/FIP200 on the ER to specify autophagosome initiation sites [90]. This proposed role for the outer surface of the ER in autophagosome biogenesis is consistent with our model in which ER dynamics is required for formation of autophagosomes. Thus, Atg9 may integrate signals of synaptic function (e.g. exo-endocytosis at synapses) with dynamic ER tubules to define sites of autophagosome biogenesis. In this model, impaired delivery of Atg9 to synapses and/or impaired ER structure (Figure 4) and dynamics (Figure 6) may underlie defective autophagosome formation in C9-ALS-FTD.

A surprising finding in our investigation of the mechanism of autophagy disruption in *Drosophila* C9-ALS-FTD models is a profound impairment in ER morphology and dynamics, not previously demonstrated in C9-ALS-FTD models. Although future studies will be required to clarify the mechanism for disrupted ER in C9-ALS-FTD, our live imaging studies of ER within motor neurons reveals key differences between the cell body and axons. Within the perinuclear soma, ER shows an interconnected reticular network with oscillating movement (Figure 6A; Movie S7), similar to movement described in nonneuronal cells [91]. In contrast, ER within axons and terminal boutons show single tubule growth and retraction, similar to movements described in the periphery of non-neuronal cells (Figure 6B,C; Movie S9,S11) [80,92]. We hypothesize that these distinct ER dynamics are due to differences in MT polarity within the soma and in axons. Indeed, recent evidence suggests that MTs regulate both ER morphology [93,94] and dynamics [95–97]. Though 30 R-expressing animals display rigid ER dynamics, we detect normal linear arreangement of MTs with intact axonal transport of autophagosomes (Figure 1) and mitochondria [71]. Interestingly, ER arrangement regulates endosomal positiong and traffic independent of MTs [32], and HSP disease mutations in RTN2 disrupt both axonal ER structure and dynamics and also trafficking of dense core vesicles [98]. In this regard, we previously showed that 30 R expression impairs axonal transport of endo-lysosomes and dense core vesicles [71]. Thus, we hypothesize that impaired ER dynamics might underlie both the impairment in synaptic autophagosome biogenesis as well as altered axonal trafficking of endo-lysosomes and other organelles.

Recently, the ER has been increasingly viewed as a hub for organelle dynamics and interactions [97,99,100]. In neurons, however, it is still not clear whether and how ER influences the dynamics of autophagosomes: from organelle formation to maturation and axonal transport. By investigating the *in vivo* spatiotemporal coordination of ER and autophagosomes in fly motor neurons, we propose that dynamic, presynaptic ER contributes to the biogenesis of distal autophagosomes (Figure 9). This proposed mechanism is based on several observation. First, an analysis of multiple mutations that disrupt axonal ER morphology also impair synaptic autophagosome formation (Figure 7), and the degree of impairment correlates with the degree of ER disruption (Fig S5F). Second, we observed co-migration of autophagosomes with dynamic ER tubules at synaptic boutons (Figure 8). Third, in 30 R-expressing motor axons, we see both a severe disruption of ER dynamics (Figure 6) as well as a severe reduction of autophagosomes at synapses (Figure 2). This model is consistent with prior evidence in cultured neurons that the biogenesis of autophagosomes is enriched in the distal axon, and that neuronal autophagosomes form at DFCP1-positive subdomains of the ER [9]. A recent study suggests that Ca^{2+} transients on the ER surface can specify autophagosome initiation sites [90], suggesting a potential mechanistic link between neuronal activity, ER-resident calcium channels, and autophagosome biogenesis.

Many ER membrane proteins, including Spastin, Atlastin, REEP and Reticulon, are known for shaping ER morphology. Notably, ER structural derangements via mutations in any one of these genes are linked to the neurodegenerative disease HSP [36–38,101]. Furthermore, mutations in another ER resident membrane protein VAPB (vesicle associated membrane protein B and C) cause familial ALS [39]. Although the mechanism whereby mutant VAPB causes motor neuron degeneration is still under debate, these mutations disrupt ER integrity and cause an accumulation of undegraded materials, likely due to autophagy dysfunction [102]. Furthermore, increasing evidence suggests that defects in autophagic flux may contribute to ALS. In addition to C9orf72 [103,104], multiple genes that cause ALS when mutated are strongly implicated in autophagy, including OPTN [105,106], TBK1 [107,108] and SQSTM1/p62 [109,110]. In addition, other ALS-linked genes such as *DCTN1* [111,112] and *VAPB* [39] have been shown to potentially affect autophagy pathway through regulating organelle dynamics.

Despite the severe impairment in ER integrity and autophagosome biogenesis that we observed in our *Drosophila* models of C9-ALS-FTD, the synaptic localization (Figure 2C,D) and axonal transport of mitochondria [71] do not appear to be disrupted, and maturation and retrograde axonal transport of autophagosomes occurs normally, consistent with the intact morphology of axonal MTs (Fig S3C). This observation suggests that during the larval stages when we perform our assays, the disruption in ER dynamics and autophagosome biogenesis occur early, prior to axonal degeneration. Our genetic epistasis experiments using Atg5 knockdown and mutations that alter ER morphology suggest that the ER phenotypes are likely upstream of the defect in autophagosome formation at synapses. However, the mechanisms underlying the severe disruption of ER morphology and dynamics in our fly C9-ALS-FTD models remains unclear and is the subject of ongoing investigations.

Materials and methods

Fly strains and larval maintenance

Drosophila melanogaster flies were reared at 25°C on standard molasses-based cornmeal agar medium supplemented with yeast. The fly crosses for GAL4-UAS system were used to express $(G_4C_2)_n$ repeats, and to visualize fluorescently labeled organelles under the control of the glutamatergic neuronal driver *VGlut-GAL4* to investigate intracellular organelle dynamics in motor neurons. All cultured larvae from experimental fly crosses were kept at 25°C except for experiments using TrpA1. For experiments using TrpA1, larvae were raised at 20°C, and placed in a moisturized 29°C heated agar medium for either 30 min or 1 h before larval dissection [18,72]. The following transgenic stocks were obtained from the Bloomington *Drosophila* Stock Center (BDSC), the Vienna *Drosophila* Resource Center (VDRC), or other sources as indicated: w^{1118} (3605), OK371-GAL4 (VGlut-GAL4) (26160), nSyb-GAL4 (51635), Mhc-GAL4 (55133), Cg-GAL4 (7011), UAS-dTrpA1 (26263 and 26,264), UAS-mito-GFP (8442 and 8443), UAS-Rab7-GFP (42705), UAS-GFP-Lamp1 (42714), UAS-sfGFP-HDEL (64748 and 64,749), UAS-GFP-KDEL (31423 and 30,903), UAS-tdTomato-sec61β (64746 and 64,747), UAS-luciferase RNAi (31603), UAS-LacZ (3956), UAS-Atg5 RNAi (27551), UAS-atl RNAi (36736), UAS-atl^{R192Q} (93456) and UAS-atl^{R214C} (93455) were obtained from the BDSC. UAS-Rtnl1 RNAi (7866) was obtained from the VDRC. UAS-mCherry-Atg8a and UAS-Atg9-GFP were obtained from T.P. Neufeld (University of Minnesota, USA). UAS-$(G_4C_2)_{30}$ was a gift from P. Jin (Emory University, USA). UAS-$(G_4C_2)_3$, UAS-RO_{36} and UAS-$(G_4C_2)_{36}$ were obtained from A.M. Isaacs (University College London, UK). UAS-LDS-$(G_4C_2)_{12}$ and UAS-LDS-$(G_4C_2)_{44}$ were kindly provided by N.M. Bonini (University of Pennsylvania, USA).

Confocal microscopy and live image acquisition

Samples were imaged on either Zeiss LSM800 or LSM880 laser scanning confocal microscope equipped with an Airyscan detector. Images were acquired by using Plan-Apochromat 63×/1.4 NA oil immersion objective with either 2× or 4× zoom, and collected through the frame size of 512 × 512pixel (50.71 µm x 50.71 µm) in 16-bit with bi-directional 2-line averaging. Late third instar larvae were rinsed in distilled water and sacrificed for imaging motor neurons with intact ventral nerve cord (VNC), segmental nerves (SNs) and neuromuscular junctions (NMJs) [11,71,113]. Selected larvae were dissected in HL3 buffer containing 0.6 mM $CaCl_2$ and 4 mM L-glutamate at room temperature, and images were immediately acquired within 20 minutes of dissection to ensure normal physiological conditions of the nervous system [11,71,114]. Temperature stimulated dTrpA1 expressing larvae were dissected in pre-heated HL3 at 30°C. Motor neuronal cell bodies were imaged from the larval VNC, while axons were observed at the middle region (~800 µm from the VNC) of the longest SN, and NMJs were monitored between muscles 6 and 7 from A6 or A7 SNs. Single motor neuron axons that are connected with synaptic terminal boutons were observed at the distal region (~100 µm from the NMJs) from A6 or A7 SNs. Time-lapse confocal images from the SNs were obtained at 1-s time intervals for 2 minutes for axonal transport analyses, while images from NMJs were obtained at 1 sec time intervals for 1 minute for analyzing distal organelle dynamics at terminal boutons. For imaging ER dynamics in motor neurons, images were taken from the VNCs, SNs and NMJs at 1 sec time intervals for 1 minute.

Immunohistochemistry

Larval dissections and immunostaining procedure were followed as previously described [11,71]. In brief, dissected animals were washed with PBS (Quality Biological, 119-069-131), and fixed in 4% paraformaldehyde for 20 minutes at room temperature. The fixed samples were permeabilized in PBS-T (PBS containing 0.1% Triton X-100 [Sigma Aldrich, 9036-19-5]) for 10 minutes and blocked with PBS-TB (PBS-T containing 2% BSA [Sigma Aldrich, 9048-46-8]) for 30 minutes at room temperature. The blocked samples were then incubated in PBS-TB with antibodies overnight at 4°C. Immunostained samples were washed 3 times (twice with PBS-TB and once with PBS in sequence) before mounting, and prepared on glass-slides in mounting medium (Vector Laboratories, H-1000; vectashield antifade mounting medium) for microscopy. For immunostaining larval autophagosomes, primary rabbit anti-DsRed antibody was used to target mCherry-Atg8a. For detecting preautophagosomal structures, primary chicken anti-GFP antibody was used to amplify Atg9-GFP$^+$ signals. Antibodies were used at the following concentrations: rabbit anti-DsRed (Takara Bio, 632496; 1:250), chicken anti-GFP (Abcam, ab13970; 1:1000), Alexa Fluor 488-conjugated goat anti-chicken (Invitrogen, A-11039; 1:500), Alexa Fluor 488-conjugated donkey anti-mouse (Life Technologies, R37114; 1:500), Alexa Fluor 546-conjugated goat anti-rabbit (Invitrogen, A-11035; 1:500), Alexa Fluor 488-conjugated goat anti-HRP (Jackson ImmunoResearch, AB-2338965; 1:1000), Alexa Fluor 594-conjugated goat anti-HRP (Jackson ImmunoResearch, AB-2338966; 1:1000), and acetyl-TUBA/α-tubulin mouse monoclonal antibody (Cell Signaling Technology, 12152S; 1:500).

In vivo *image processing and axonal transport analyses*

To determine the number of organelles in motor axons, the second frame from the acquired time-lapse images was selected for quantification. Either Zeiss Zen Blue or Zeiss Zen Black 2.3 software was used for detecting autophagic vacuoles, and the following thresholds for each positive fluorescent signal (mCherry or GFP) were used to determine as individual vesicle or organelle in the region of observation: autophagosome (mCherry-Atg8a ≥300), late endosome (Rab7-GFP ≥500) and lysosome (GFP-Lamp1 ≥ 500) in 16-bit range with an adapted gamma value of 1.20. Spot analysis by using TrackMate Plugins in ImageJ Fiji software was used for auto-detection of axonal autophagosomes, and the DoG detector at following thresholds for mCherry-Atg8a was used to determine an individual autophagosome in the region of observation: blob diameter (0.7 µm, in a median filter threshold as 2.0) with spot (filter quality ≥ 10).

To analyze axonal transport of autophagic vesicles, the acquired time-lapse confocal images were pre-calibrated using Image Stabilizer in ImageJ Fiji software. Axonal transport quantification was performed as previously described using manual tracking in ImageJ Fiji software: flux, moving and stationary %, duty cycle, run length and velocity [11,71,114]. For flux measurement, two defined points were designated within the observed axon using Zeiss Zen software, and the counted numbers of moving organelles/vesicles passing the defined points were averaged for both anterograde and retrograde movement. For measuring moving and stationary %, the total population of organelles acquired from the second frame of the time-lapse images was used, and categorized as anterograde, retrograde or stationary using Cell Counter in ImageJ Fiji software. To measure duty cycle, run length or velocity, organelles/vesicles were considered for axonal transport analysis only if they could be continuously tracked for more than 60 frames. Since one pixel represents 0.099 µm in our image acquisition, only net velocities greater than 0.1 µm/s with more than 3 consecutive frames in one direction were selected as bona fide anterograde or retrograde movement. At least 5 organelles/vesicles per animal were selected for axonal transport analyses, and the representative kymographs were generated using either Zeiss Zen Blue or Zeiss Zen Black software.

Image processing and organelle verification

For determination of organelle density and co-localization, Imaris x64 9.0.1 software was used, and the designated region of motor neuronal axons and/or synaptic terminal boutons was analyzed either from stacked time series or from selected 2-dimensional images. To measure organelle density, an individual polygon is manually created to set region of interest (ROI), and volumetric measurement by Surface Segmentation using Imaris was applied with the following criteria: surface detail of 0.08 μm for synaptic boutons, and surface detail of 0.1 μm for organelles followed by smooth quality processing. The absolute signal intensity threshold within created ROI was varied to cover the surface of a single terminal bouton and/or organelle individually, and IsoSurface for each channel was created under Surpass Tree to measure the covered area by each signal. To determine organelle co-localization, spot detection in XT functions from Imaris was applied, and IsoSpot for each channel was created under Surpass Tree. MATLAB R2015a linked to Imaris x64 9.0.1 software was utilized for counting spots and spot co-localization measurement with the following thresholds: spot (0.8 μm diameter with quality ≥ 7) for organelle recognition, and spot distance (≤ 1) for defining co-localization. At least 3 boutons and/or 2 axons per animal were selected for verifying organelle density and co-localization.

Image processing and ER morphology quantification

Drosophila larval motor neurons expressing sfGFP-HDEL driven by *VGlut-GAL4* were monitored to verify ER structure, and motor neuronal cell bodies from VNC and synaptic terminal boutons at the NMJ were selected for ER morphology determination. ER structure in motor neuronal cell bodies was also verified from the adult VNC by sacrificing unhatched flies in pupal cases and dissecting their thorax. In cell bodies, to parameterize the ER shape and/or structure, ER network segmentation was skeletonized for quantification of ER tubule three-way junction (3WJ) density. To quantify 3WJs, the acquired images were binarized with open processing and outlier noise removed by 2.0 pixel radius, and then images were skeletonized and classified into each branch using Skeleton Plugin in ImageJ Fiji. Only the longest branch among the skeleton was considered for 3WJ quantification to avoid misreading of ER branch from the adjacent cell body. 3WJ quantification was conducted by measuring the number of 3WJs per ER tubule length. In synaptic terminal boutons, ER structure was determined by quantifying ER fragmentation. ROI for synaptic terminal boutons was designated by *in vivo* staining with anti-HRP to label neuronal membranes, and the number of punctate ER fragments per bouton was measured for ER morphology quantification in motor neuronal synaptic terminal boutons. ER morphology in larval fat bodies and muscle cells was monitored driven by *Cg-GAL4* and *Mhc-GAL4*, respectively. To analyze ER structure in larval muscle cells, longitudinal muscles either 6 or 7 in A4 segment were selected, and periodic organization of sarcoplasmic reticulum was identified by measuring horizontal (anteroposterior axis) and vertical (lateral axis) distances.

In vivo *image processing and analysis of ER dynamics*

Neuronal ER dynamics were obtained in cell bodies from VNC, in axons from SN, and in synaptic terminal boutons from the NMJ, respectively. The regions from acquired time-lapse image where the ER tubules and/or network could be continuously resolved in a single plane of view were considered for analyses of ER dynamics. To quantify the dynamics of the ER network in motor neuronal cell bodies, the acquired time-lapse confocal images were stabilized with surface binary processing using ImageJ Fiji. The calibrated time-lapse images were then imported to Imaris x64 9.0.1 software for image pre-correction through background subtraction (estimated XY diameter in 0.35 μm) without smoothing. Individual frames were subtracted from the corrected images and coded for pseudo-color masking. The color-coded frames were converted to surface channels separately, and then merged into one by using Surface Segmentation in Imaris to get co-localization data per time points. Pearson coefficients were measured to quantify linear correlation between two-color variables in every 10 sec time-lag from the combined channels. At least 3 motor neuron cell bodies were monitored from the VNC per animal. To verify axonal ER dynamics, time-lapse images were processed under Slice Representation and adjusted through Deconvolution Sharpening using Imaris with the following parameters: deconvolution parameters set in Advanced with Robust (iterative) algorithm. Pre-sharpening gain was varied (5–15%) to improve the contrast and resolution of reconstructed distal images. Within the branched axonal ER, either ER tubule elongation or shrinkage greater than 2 μm with more than 3 consecutive frames in one direction were defined as bona fide ER tubule growth or retraction. Axonal ER tubule discontinuity was defined as ER tubule fragmentation that appeared for more than 10 consecutive frames. At least 2 regions from the longest SN per animal were monitored for axonal ER dynamics analysis. To quantify dynamics of terminal bouton ER, terminal ER tubulation was monitored in motor neuron synaptic boutons at the NMJ, and tubulation was observed by measuring the number of events of ER tubule growth and retraction. The acquired time-lapse confocal images were stabilized, and edge detected through Canny-Deriche filtering (alpha parameter from 0.5 to 1.2) using ImageJ Fiji before quantification. Manually created elliptical selection of ROIs were applied within the observed single bouton, and ER tubules crossing the defined ROIs for more than 3 sec continuously in one direction were designated as ER tubule growth or ER tubule retraction. Terminal ER fragmentation was defined as punctate ER that appeared for more than 10 consecutive frames, and the ER fragments were considered as static particles when they displayed restricted movement within 0.25 μm radius for more than 10 s. Within synaptic boutons, only terminal boutons were monitored, and at least 2 terminal boutons per animal were analyzed for the terminal ER dynamics.

Quantitative RT-PCR analysis

For each genotype, pan-neuronal *nSyb-GAL4* was used to express the gene of interest. Total RNA was isolated from 24 larval brains containing brain lobes and VNC by using miRNeasy Mini Kit (Qiagen, 217004) according to the manufacturer's protocol. RNA concentration was measured using a spectrophotometer (NanoDrop 2000c) and reverse transcription was performed using ProtoScript II First Strand cDNA Synthesis Kit (Life Technologies, E6560S) following the manufacturer's instructions. Quantitative PCR was performed using SYBR Green PCR system (Applied Biosystems, A25741) on a QuantStudio 3 fast Real-time PCR system (Applied Biosystems, A28136). Actin was used as a reference gene for relative quantification and the primers used to amplify either *Act* (Actin) or the *Atg5* gene were as follows: *Act* forward (5'-GCGCGGTTACTCTTTCACCA-3'), *Act* reverse (5'-ATGTCACGGACGATTTCACG-3'), *Atg5* forward (5'-GCACTACATGTCCTGCCTGA-3') and *Atg5* reverse (5'-AGATTCGCAGGGGAATGTTT-3') [83].

Statistical analysis

GraphPad Prism 8 (Version 8.4.2) was used to generate graphical display of the data, and to perform statistical analyses. For comparison of two groups, an unpaired homoscedastic *t*-test was used. For multiple group comparisons, one-way ANOVA with a Bonferroni correction (Bonferroni *post-hoc* test) was applied as indicated in each figure legend. For the multiple subgroup comparision, Chi-Square test with a *post-hoc* analysis was performed to examine the frequencies of nominal categories for anterograde, retrograde and stationary. Boxplots were depicted by drawing the first and third quartile with the horizontal bar at the median and whiskers showing the most extreme data points. Bar graphs display mean ± SEM. The number (n) of biological samples used in each experiment is indicated in each figure legend. In all cases, at least three independent experiments were performed, and the data quantification was performed with blinded analysis. In all analyses, significance is expressed as p values, and the difference between groups was defined as statistically significant for the following p values: * < 0.05, ** < 0.01, *** < 0.001 and **** < 0.0001.

Acknowledgements

We thank Thomas Neufeld, Peng Jin, Adrian Isaacs and Nancy Bonini for providing *Drosophila* reagents, and thank Matthew Goynatsky, Sarah Berth and Andrew Cheng for assistance with blinded analyses. We specially thank Michele Pucak and the NINDS Multi-photon Imaging (MPI) Core Facility (NS050274) at JHMI for supporting image services.

Disclosure statement

No potential conflict of interest was reported by the authors.

Funding

This work was supported by NIH/NINDS (R01NS094239), ALS Association and Robert Packard Center for ALS.

ORCID

Hyun Sung http://orcid.org/0000-0003-3451-1442
Thomas E. Lloyd http://orcid.org/0000-0003-4756-3700

References

[1] Damme M, Suntio T, Saftig P, et al. Autophagy in neuronal cells: general principles and physiological and pathological functions. Acta Neuropathol. 2015 Mar;129(3):337–362. doi: 10.1007/s00401-014-1361-4
[2] Maday S. Mechanisms of neuronal homeostasis: autophagy in the axon. Brain Res. 2016 Oct 15;1649(Pt B):143–150.
[3] Stavoe AKH, Holzbaur ELF. Autophagy in neurons. Annu Rev Cell Dev Biol. 2019 Oct 6;35(1):477–500.
[4] Stavoe AKH, Holzbaur ELF. Axonal autophagy: mini-review for autophagy in the CNS. Neurosci Lett. 2019 Apr 1;697:17–23. doi: 10.1016/j.neulet.2018.03.025.
[5] Komatsu M, Waguri S, Chiba T, et al. Loss of autophagy in the central nervous system causes neurodegeneration in mice. Nature. 2006 Jun 15;441(7095):880–884.
[6] Nixon RA. The role of autophagy in neurodegenerative disease. Nat Med. 2013 Aug;19(8):983–997. doi: 10.1038/nm.3232
[7] Park H, Kang JH, Lee S. Autophagy in neurodegenerative diseases: a hunter for aggregates. Int J Mol Sci. 2020 May 10;21(9):3369.
[8] Watanabe Y, Taguchi K, Tanaka TM. Ubiquitin, autophagy and neurodegenerative diseases. Cells. 2020 Sep 2;9(9):2022.
[9] Maday S, Holzbaur EL. Autophagosome biogenesis in primary neurons follows an ordered and spatially regulated pathway. Dev Cell. 2014 Jul 14;30(1):71–85. doi: 10.1016/j.devcel.2014.06.001
[10] Maday S, Holzbaur EL. Compartment-specific regulation of autophagy in primary neurons. J Neurosci. 2016 Jun 1;36(22):5933–5945.
[11] Sung H, Tandarich LC, Nguyen K, et al. Compartmentalized regulation of parkin-mediated mitochondrial quality control in the Drosophila nervous System in vivo. J Neurosci. 2016 Jul 13;36(28):7375–7391.
[12] Evans CS, Holzbaur EL. Degradation of engulfed mitochondria is rate-limiting in optineurin-mediated mitophagy in neurons. Elife. 2020 Jan 14; 9. doi: 10.7554/eLife.50260.
[13] Johnson DE, Ostrowski P, Jaumouille V, et al. The position of lysosomes within the cell determines their luminal pH. J Cell Bio. 2016 Mar 14;212(6):677–692.
[14] Overly CC, Lee KD, Berthiaume E, et al. Quantitative measurement of intraorganelle pH in the endosomal-lysosomal pathway in neurons by using ratiometric imaging with pyranine. Proc Natl Acad Sci U S A. 1995 Apr 11;92(8):3156–3160.
[15] Parton RG, Simons K, Dotti CG. Axonal and dendritic endocytic pathways in cultured neurons. J Cell Bio. 1992 Oct;119(1):123–137. doi: 10.1083/jcb.119.1.123
[16] Maday S, Wallace KE, Holzbaur EL. Autophagosomes initiate distally and mature during transport toward the cell soma in primary neurons. J Cell Bio. 2012 Feb 20;196(4):407–417.
[17] Neisch AL, Neufeld TP, Hays TS. A STRIPAK complex mediates axonal transport of autophagosomes and dense core vesicles through PP2A regulation. J Cell Bio. 2017 Feb;216(2):441–461. doi: 10.1083/jcb.201606082
[18] Soukup SF, Kuenen S, Vanhauwaert R, et al. A LRRK2-dependent Endophilin A phosphoswitch is critical for macroautophagy at presynaptic terminals. Neuron. 2016 Nov 23;92(4):829–844.
[19] Stavoe AK, Hill SE, Hall DH, et al. KIF1A/UNC-104 transports ATG-9 to regulate neurodevelopment and autophagy at synapses. Dev Cell. 2016 Jul 25;38(2):171–185.
[20] Vukoja A, Rey U, Petzoldt AG, et al. Presynaptic biogenesis requires axonal transport of lysosome-related vesicles. Neuron. 2018 Sep 19;99(6):1216–1232 e7.
[21] Alirezaei M, Kemball CC, Flynn CT, et al. Short-term fasting induces profound neuronal autophagy. Autophagy. 2010 Aug;6(6):702–710. doi: 10.4161/auto.6.6.12376
[22] Yang Z, Klionsky DJ. Mammalian autophagy: core molecular machinery and signaling regulation. Curr Opin Cell Biol. 2010 Apr;22(2):124–131. doi: 10.1016/j.ceb.2009.11.014
[23] Young JE, Martinez RA, La Spada AR. Nutrient deprivation induces neuronal autophagy and implicates reduced insulin signaling in neuroprotective autophagy activation. J Biol Chem. 2009 Jan 23;284(4):2363–2373.
[24] Juhasz G, Neufeld TP. Autophagy: a forty-year search for a missing membrane source. PLoS Biol. 2006 Feb;4(2):e36. doi: 10.1371/journal.pbio.0040036
[25] Nascimbeni AC, Codogno P, Morel E. Local detection of PtdIns3P at autophagosome biogenesis membrane platforms. Autophagy. 2017 Sep 2;13(9):1602–1612.

[26] Tooze SA. Current views on the source of the autophagosome membrane. Essays Biochem. 2013;55:29–38. doi: 10.1042/bse0550029
[27] Ozturk Z, O'Kane CJ, Perez-Moreno JJ. Axonal endoplasmic reticulum dynamics and its Roles in neurodegeneration. Front Neurosci. 2020;14:48. doi: 10.3389/fnins.2020.00048
[28] Ktistakis NT. ER platforms mediating autophagosome generation. Biochim Biophys Acta, Mol Cell Biol Lipids. 2020 Jan;1865 (1):158433. doi: 10.1016/j.bbalip.2019.03.005
[29] Axe EL, Walker SA, Manifava M, et al. Autophagosome formation from membrane compartments enriched in phosphatidylinositol 3-phosphate and dynamically connected to the endoplasmic reticulum. J Cell Bio. 2008 Aug 25;182(4):685–701.
[30] Melani M, Valko A, Romero NM, et al. Zonda is a novel early component of the autophagy pathway in Drosophila. Mol Biol Cell. 2017 Nov 1;28(22):3070–3081.
[31] Nishimura T, Tamura N, Kono N, et al. Autophagosome formation is initiated at phosphatidylinositol synthase-enriched ER subdomains. EMBO J. 2017 Jun 14;36(12):1719–1735.
[32] Friedman JR, Dibenedetto JR, West M, et al. Endoplasmic reticulum-endosome contact increases as endosomes traffic and mature. Mol Biol Cell. 2013 Apr;24(7):1030–1040. doi: 10.1091/mbc.e12-10-0733
[33] Pankiv S, Alemu EA, Brech A, et al. FYCO1 is a Rab7 effector that binds to LC3 and PI3P to mediate microtubule plus end-directed vesicle transport. J Cell Bio. 2010 Jan 25;188(2):253–269.
[34] Rocha N, Kuijl C, van der Kant R, et al. Cholesterol sensor ORP1L contacts the ER protein VAP to control Rab7-RILP-p150 glued and late endosome positioning. J Cell Bio. 2009 Jun 29;185(7):1209–1225.
[35] Nakashima A, Cheng SB, Kusabiraki T, et al. Endoplasmic reticulum stress disrupts lysosomal homeostasis and induces blockade of autophagic flux in human trophoblasts. Sci Rep. 2019 Aug 7;9(1):11466.
[36] Esteves T, Durr A, Mundwiller E, et al. Loss of association of REEP2 with membranes leads to hereditary spastic paraplegia. Am J Hum Genet. 2014 Feb 6;94(2):268–277.
[37] Montenegro G, Rebelo AP, Connell J, et al. Mutations in the ER-shaping protein reticulon 2 cause the axon-degenerative disorder hereditary spastic paraplegia type 12. J Clin Invest. 2012 Feb;122(2):538–544. doi: 10.1172/JCI60560
[38] Zhao X, Alvarado D, Rainier S, et al. Mutations in a newly identified GTPase gene cause autosomal dominant hereditary spastic paraplegia. Nat Genet. 2001 Nov;29(3):326–331. doi: 10.1038/ng758
[39] Nishimura AL, Mitne-Neto M, Silva HC, et al. A mutation in the vesicle-trafficking protein VAPB causes late-onset spinal muscular atrophy and amyotrophic lateral sclerosis. Am J Hum Genet. 2004 Nov;75(5):822–831. doi: 10.1086/425287
[40] Yamanaka T, Nishiyama R, Shimogori T, et al. Proteomics-based approach identifies altered ER domain properties by ALS-Linked VAPB mutation. Sci Rep. 2020 May 6;10(1):7610.
[41] Al-Chalabi A, Hardiman O. The epidemiology of ALS: a conspiracy of genes, environment and time. Nat Rev Neurol. 2013 Nov;9(11):617–628. doi: 10.1038/nrneurol.2013.203
[42] Pasinelli P, Brown RH. Molecular biology of amyotrophic lateral sclerosis: insights from genetics. Nat Rev Neurosci. 2006 Sep;7 (9):710–723. doi: 10.1038/nrn1971
[43] Rowland LP, Shneider NA. Amyotrophic lateral sclerosis. N Engl J Med. 2001 May 31;344(22):1688–1700.
[44] Abramzon YA, Fratta P, Traynor BJ, et al. The overlapping genetics of amyotrophic lateral sclerosis and frontotemporal dementia. Front Neurosci. 2020;14:42. doi: 10.3389/fnins.2020.00042
[45] Beckers J, Tharkeshwar AK, Van Damme P. C9orf72 ALS-FTD: recent evidence for dysregulation of the autophagy-lysosome pathway at multiple levels. Autophagy. 2021 Nov;17(11):3306–3322. doi: 10.1080/15548627.2021.1872189
[46] Ling SC, Polymenidou M, Cleveland DW. Converging mechanisms in ALS and FTD: disrupted RNA and protein homeostasis. Neuron. 2013 Aug 7;79(3):416–438.
[47] Arai T, Hasegawa M, Akiyama H, et al. TDP-43 is a component of ubiquitin-positive tau-negative inclusions in frontotemporal lobar degeneration and amyotrophic lateral sclerosis. Biochem Biophys Res Commun. 2006 Dec 22;351(3):602–611.
[48] Blokhuis AM, Groen EJ, Koppers M, et al. Protein aggregation in amyotrophic lateral sclerosis. Acta Neuropathol. 2013 Jun;125 (6):777–794. doi: 10.1007/s00401-013-1125-6
[49] Lin G, Mao D, Bellen HJ. Amyotrophic lateral sclerosis pathogenesis converges on defects in protein homeostasis associated with TDP-43 mislocalization and proteasome-mediated degradation overload. Curr Top Dev Biol. 2017;121:111–171.
[50] Neumann M, Sampathu DM, Kwong LK, et al. Ubiquitinated TDP-43 in frontotemporal lobar degeneration and amyotrophic lateral sclerosis. Science. 2006 Oct 6;314 (5796):130–133.
[51] DeJesus-Hernandez M, Mackenzie IR, Boeve BF, et al. Expanded GGGGCC hexanucleotide repeat in noncoding region of C9ORF72 causes chromosome 9p-linked FTD and ALS. Neuron. 2011 Oct 20;72(2):245–256.
[52] Renton AE, Majounie E, Waite A, et al. A hexanucleotide repeat expansion in C9ORF72 is the cause of chromosome 9p21-linked ALS-FTD. Neuron. 2011 Oct 20;72(2):257–268.
[53] Waite AJ, Baumer D, East S, et al. Reduced C9orf72 protein levels in frontal cortex of amyotrophic lateral sclerosis and frontotemporal degeneration brain with the C9ORF72 hexanucleotide repeat expansion. Neurobiol Aging. 2014 Jul;35(7):e1779 5–e1779 13. doi: 10.1016/j.neurobiolaging.2014.01.016
[54] Donnelly CJ, Zhang PW, Pham JT, et al. RNA toxicity from the ALS/FTD C9ORF72 expansion is mitigated by antisense intervention. Neuron. 2013 Oct 16;80(2):415–428.
[55] Haeusler AR, Donnelly CJ, Periz G, et al. C9orf72 nucleotide repeat structures initiate molecular cascades of disease. Nature. 2014 Mar 13;507(7491):195–200.
[56] Lee YB, Chen HJ, Peres JN, et al. Hexanucleotide repeats in ALS/FTD form length-dependent RNA foci, sequester RNA binding proteins, and are neurotoxic. Cell Rep. 2013 Dec 12;5 (5):1178–1186.
[57] Ash PE, Bieniek KF, Gendron TF, et al. Unconventional translation of C9ORF72 GGGGCC expansion generates insoluble polypeptides specific to c9FTD/ALS. Neuron. 2013 Feb 20;77(4):639–646.
[58] Mori K, Weng SM, Arzberger T, et al. The C9orf72 GGGGCC repeat is translated into aggregating dipeptide-repeat proteins in FTLD/ALS. Science. 2013 Mar 15;339(6125):1335–1338.
[59] Zu T, Liu Y, Banez-Coronel M, et al. RAN proteins and RNA foci from antisense transcripts in C9ORF72 ALS and frontotemporal dementia. Proc Natl Acad Sci U S A. 2013 Dec 17;110(51): E4968–77.
[60] Zhang K, Donnelly CJ, Haeusler AR, et al. The C9orf72 repeat expansion disrupts nucleocytoplasmic transport. Nature. 2015 Sep 3;525(7567):56–61.
[61] Cunningham KM, Maulding K, Ruan K, et al. Tfeb/mitf links impaired nuclear import to autophagolysosomal dysfunction in C9-ALS. Elife. 2020 Dec 10;9. doi:10.7554/eLife.59419
[62] Cai Y, Arikkath J, Yang L, et al. Interplay of endoplasmic reticulum stress and autophagy in neurodegenerative disorders. Autophagy. 2016;12(2):225–244. doi: 10.1080/15548627.2015.1121360
[63] Hetz C, Thielen P, Matus S, et al. XBP-1 deficiency in the nervous system protects against amyotrophic lateral sclerosis by increasing autophagy. Genes Dev. 2009 Oct 1;23(19):2294–2306.
[64] Guo W, Stoklund Dittlau K, Van Den Bosch L. Axonal transport defects and neurodegeneration: molecular mechanisms and therapeutic implications. Semin Cell Dev Biol. 2020 Mar;99:133–150. doi: 10.1016/j.semcdb.2019.07.010
[65] Sleigh JN, Rossor AM, Fellows AD, et al. Axonal transport and neurological disease. Nat Rev Neurol. 2019 Dec;15(12):691–703. doi: 10.1038/s41582-019-0257-2
[66] De Vos KJ, Hafezparast M. Neurobiology of axonal transport defects in motor neuron diseases: opportunities for translational research? Neurobiol Dis. 2017 Sep;105:283–299. doi: 10.1016/j.nbd.2017.02.004

[67] Mizielinska S, Gronke S, Niccoli T, et al. C9orf72 repeat expansions cause neurodegeneration in Drosophila through arginine-rich proteins. Science. 2014 Sep 5;345(6201):1192–1194.
[68] Vijayan V, Verstreken P. Autophagy in the presynaptic compartment in health and disease. J Cell Bio. 2017 Jul 3;216 (7):1895–1906.
[69] He C, Song H, Yorimitsu T, et al. Recruitment of Atg9 to the preautophagosomal structure by Atg11 is essential for selective autophagy in budding yeast. J Cell Bio. 2006 Dec 18;175 (6):925–935.
[70] Yang S, Park D, Manning L, et al. Presynaptic autophagy is coupled to the synaptic vesicle cycle via ATG-9. Neuron. 2022 Mar 2;110(5):824–840 e10.
[71] Sung H, Lloyd TE. Defective axonal transport of endo-lysosomes and dense core vesicles in a Drosophila model of C9-ALS/FTD. Traffic. 2022 Sep;23(9):430–441. doi: 10.1111/tra.12861
[72] Pulver SR, Pashkovski SL, Hornstein NJ, et al. Temporal dynamics of neuronal activation by channelrhodopsin-2 and TRPA1 determine behavioral output in Drosophila larvae. J Neurophysiol. 2009 Jun;101(6):3075–3088. doi: 10.1152/jn.00071.2009
[73] Pankiv S, Clausen TH, Lamark T, et al. p62/SQSTM1 binds directly to Atg8/LC3 to facilitate degradation of ubiquitinated protein aggregates by autophagy. J Biol Chem. 2007 Aug 17;282(33):24131–24145.
[74] Cheng XT, Zhou B, Lin MY, et al. Axonal autophagosomes recruit dynein for retrograde transport through fusion with late endosomes. J Cell Bio. 2015 May 11;209(3):377–386.
[75] Moustaqim-Barrette A, Lin YQ, Pradhan S, et al. The amyotrophic lateral sclerosis 8 protein, VAP, is required for ER protein quality control. Hum Mol Genet. 2014 Apr 15;23(8):1975–1989.
[76] Yang YS, Harel NY, Strittmatter SM. Reticulon-4A (Nogo-A) redistributes protein disulfide isomerase to protect mice from SOD1-dependent amyotrophic lateral sclerosis. J Neurosci. 2009 Nov 4;29(44):13850–13859.
[77] Summerville JB, Faust JF, Fan E, et al. The effects of ER morphology on synaptic structure and function in Drosophila melanogaster. J Cell Sci. 2016 Apr 15;129(8):1635–1648.
[78] Yalcin B, Zhao L, Stofanko M, et al. Modeling of axonal endoplasmic reticulum network by spastic paraplegia proteins. Elife. 2017 Jul 25;6. doi:10.7554/eLife.23882
[79] Espadas J, Pendin D, Bocanegra R, et al. Dynamic constriction and fission of endoplasmic reticulum membranes by reticulon. Nat Commun. 2019 Nov 22;10(1):5327.
[80] Georgiades P, Allan VJ, Wright GD, et al. The flexibility and dynamics of the tubules in the endoplasmic reticulum. Sci Rep. 2017 Nov 28;7(1):16474.
[81] Perkins HT, Allan V. Intertwined and finely balanced: endoplasmic reticulum morphology, dynamics, function, and diseases. Cells. 2021 Sep 7;10(9):2341.
[82] Kuijpers M, Kochlamazashvili G, Stumpf A, et al. Neuronal autophagy regulates presynaptic neurotransmission by controlling the axonal endoplasmic reticulum. Neuron. 2021 Jan 20;109(2):299–313 e9.
[83] Ren C, Finkel SE, Tower J. Conditional inhibition of autophagy genes in adult Drosophila impairs immunity without compromising longevity. Exp Gerontol. 2009 Mar;44(3):228–235. doi: 10.1016/j.exger.2008.10.002
[84] Behrendt L, Hoischen C, Kaether C. Disease-causing mutated ATLASTIN 3 is excluded from distal axons and reduces axonal autophagy. Neurobiol Dis. 2021 Jul;155:105400. doi: 10.1016/j.nbd.2021.105400
[85] Liu N, Zhao H, Zhao YG, et al. Atlastin 2/3 regulate ER targeting of the ULK1 complex to initiate autophagy. J Cell Bio. 2021 Jul 5;220(7): doi: 10.1083/jcb.202012091
[86] Wang R, Miao G, Shen JL, et al. ESCRT dysfunction compromises endoplasmic reticulum maturation and autophagosome biogenesis in Drosophila. Curr Biol. 2022 Mar 28;32(6):1262–1274 e4.
[87] Montagna A, Vajente N, Pendin D, et al. In vivo analysis of CRISPR/Cas9 induced atlastin pathological mutations in Drosophila. Front Neurosci. 2020;14:547746. doi: 10.3389/fnins.2020.547746
[88] Hill SE, Colon-Ramos DA. The journey of the synaptic autophagosome: a cell biological perspective. Neuron. 2020 Mar 18;105(6):961–973.
[89] Sidibe DK, Vogel MC, Maday S. Organization of the autophagy pathway in neurons. Curr Opin Neurobiol. 2022 Aug;75:102554. doi: 10.1016/j.conb.2022.102554
[90] Zheng Q, Chen Y, Chen D, et al. Calcium transients on the ER surface trigger liquid-liquid phase separation of FIP200 to specify autophagosome initiation sites. Cell. 2022 Oct 27;185(22):4082–4098 e22.
[91] Janota CS, Pinto A, Pezzarossa A, et al. Shielding of actin by the endoplasmic reticulum impacts nuclear positioning. Nat Commun. 2022 May 19;13(1):2763.
[92] Nixon-Abell J, Obara CJ, Weigel AV, et al. Increased spatiotemporal resolution reveals highly dynamic dense tubular matrices in the peripheral ER. Science. 2016 Oct 28;354(6311):aaf3928–aaf3928.
[93] Grigoriev I, Gouveia SM, van der Vaart B, et al. STIM1 is a MT-plus-end-tracking protein involved in remodeling of the ER. Curr Biol. 2008 Feb 12;18(3):177–182.
[94] Zheng P, Obara CJ, Szczesna E, et al. ER proteins decipher the tubulin code to regulate organelle distribution. Nature. 2022 Jan;601(7891):132–138. doi: 10.1038/s41586-021-04204-9
[95] Stadler L, Speckner K, Weiss M. Diffusion of exit sites on the endoplasmic reticulum: a random walk on a shivering backbone. Biophys J. 2018 Oct 16;115(8):1552–1560.
[96] Friedman JR, Webster BM, Mastronarde DN, et al. ER sliding dynamics and ER-mitochondrial contacts occur on acetylated microtubules. J Cell Bio. 2010 Aug 9;190(3):363–375.
[97] Guo Y, Li D, Zhang S, et al. Visualizing intracellular organelle and cytoskeletal interactions at nanoscale resolution on millisecond timescales. Cell. 2018 Nov 15;175(5):1430–1442 e17.
[98] Zamponi E, Meehl JB, Voeltz GK. The ER ladder is a unique morphological feature of developing mammalian axons. Dev Cell. 2022 Jun 6;57(11):1369–1382 e6.
[99] Friedman JR, Lackner LL, West M, et al. ER tubules mark sites of mitochondrial division. Science. 2011 Oct 21;334(6054):358–362.
[100] Rowland AA, Chitwood PJ, Phillips MJ, et al. ER contact sites define the position and timing of endosome fission. Cell. 2014 Nov 20;159(5):1027–1041.
[101] Hazan J, Fonknechten N, Mavel D, et al. Spastin, a new AAA protein, is altered in the most frequent form of autosomal dominant spastic paraplegia. Nat Genet. 1999 Nov;23(3):296–303. doi: 10.1038/15472
[102] Tudor EL, Galtrey CM, Perkinton MS, et al. Amyotrophic lateral sclerosis mutant vesicle-associated membrane protein-associated protein-B transgenic mice develop TAR-DNA-binding protein-43 pathology. Neuroscience. 2010 May 19;167(3):774–785.
[103] Sullivan PM, Zhou X, Robins AM, et al. The ALS/FTLD associated protein C9orf72 associates with SMCR8 and WDR41 to regulate the autophagy-lysosome pathway. Acta Neuropathol Commun. 2016 May 18;4(1):51.
[104] Yang M, Liang C, Swaminathan K, et al. A C9ORF72/SMCR8-containing complex regulates ULK1 and plays a dual role in autophagy. Sci Adv. 2016 Sep;2(9):e1601167. doi: 10.1126/sciadv.1601167
[105] Korac J, Schaeffer V, Kovacevic I, et al. Ubiquitin-independent function of optineurin in autophagic clearance of protein aggregates. J Cell Sci. 2013 Jan 15;126(Pt 2):580–592.
[106] Wong YC, Holzbaur EL. Optineurin is an autophagy receptor for damaged mitochondria in parkin-mediated mitophagy that is disrupted by an ALS-linked mutation. Proc Natl Acad Sci U S A. 2014 Oct 21;111(42):E4439–48.
[107] Lazarou M, Sliter DA, Kane LA, et al. The ubiquitin kinase PINK1 recruits autophagy receptors to induce mitophagy. Nature. 2015 Aug 20;524(7565):309–314.
[108] Moore AS, Holzbaur EL. Dynamic recruitment and activation of ALS-associated TBK1 with its target optineurin are required for efficient mitophagy. Proc Natl Acad Sci U S A. 2016 Jun 14;113(24):E3349–58.
[109] Gal J, Strom AL, Kwinter DM, et al. Sequestosome 1/p62 links familial ALS mutant SOD1 to LC3 via an

ubiquitin-independent mechanism. J Neurochem. 2009 Nov;111 (4):1062–1073. doi: 10.1111/j.1471-4159.2009.06388.x

[110] Rudnick ND, Griffey CJ, Guarnieri P, et al. Distinct roles for motor neuron autophagy early and late in the SOD1(G93A) mouse model of ALS. Proc Natl Acad Sci U S A. 2017 Sep 26;114(39):E8294–E8303.

[111] Laird FM, Farah MH, Ackerley S, et al. Motor neuron disease occurring in a mutant dynactin mouse model is characterized by defects in vesicular trafficking. J Neurosci. 2008 Feb 27;28(9):1997–2005.

[112] Munch C, Sedlmeier R, Meyer T, et al. Point mutations of the p150 subunit of dynactin (DCTN1) gene in ALS. Neurology. 2004 Aug 24;63(4):724–726.

[113] Shidara Y, Hollenbeck PJ. Defects in mitochondrial axonal transport and membrane potential without increased reactive oxygen species production in a Drosophila model of Friedreich ataxia. J Neurosci. 2010 Aug 25;30(34):11369–11378.

[114] Devireddy S, Sung H, Liao PC, et al. Analysis of mitochondrial traffic in Drosophila. Methods Enzymol. 2014;547:131–150.